Functional interdependence of the actin regulators CAP1 and cofilin1 in control of dendritic spine morphology

Anika Heinze
Philipps-Universität Marburg: Philipps-Universitat Marburg
Cara Schuldt
Philipps-Universität Marburg: Philipps-Universitat Marburg
Sharof Khudayberdiev
Philipps-Universitat Marburg Universitatsbibliothek: Philipps-Universitat Marburg
Bas van Bommel
ZMNH: Universitatsklinikum Hamburg-Eppendorf Zentrum fur Molekulare Neurobiologie Hamburg
Daniela Hacker
ZMNH: Universitatsklinikum Hamburg-Eppendorf Zentrum fur Molekulare Neurobiologie Hamburg
Toni Schulz
Philipps-Universität Marburg: Philipps-Universitat Marburg
Ramona Stringhi
Università degli Studi di Milano: Universita degli Studi di Milano
Elena Marcello
Università degli Studi di Milano: Universita degli Studi di Milano
Marina Mikhaylova
ZMNH: Universitatsklinikum Hamburg-Eppendorf Zentrum fur Molekulare Neurobiologie Hamburg
Marco Rust (marco.rust@staff.uni-marburg.de)
Philipps-Universitat Marburg https://orcid.org/0000-0003-2737-1250

Research Article

Keywords: CAP1, actin dynamics, dendritic spine, cofilin, cyclase-associated protein

Posted Date: January 7th, 2022

DOI: https://doi.org/10.21203/rs.3.rs-1198887/v1

Research article, submitted to the *Cell Mol Life Sci*

Functional interdependence of the actin regulators CAP1 and cofilin1 in control of dendritic spine morphology

Anika Heinze[1,2], Cara Schuldt[1,2], Sharof Khudayberdiev[1,2], Bas van Bommel[3,§], Daniela Hacker[3,4], Toni G. Schulz[1], Ramona Stringhi[5], Elena Marcello[5], Marina Mikhaylova[3,4], Marco B. Rust[1,2,6,*]

[1]Molecular Neurobiology Group, Institute of Physiological Chemistry, Philipps-University of Marburg, 35032 Marburg, Germany; [2]Center for Mind, Brain and Behavior (CMBB), University of Marburg and Justus-Liebig-University Giessen, 35032 Marburg, Germany; [3]AG Optobiology, Institute of Biology, Humboldt-University, 10115 Berlin, Germany; [4]DFG Emmy Noether Guest Group 'Neuronal Protein Transport', Institute for Molecular Neurogenetics, Center for Molecular Neurobiology (ZMNH), University Medical Center Hamburg-Eppendorf (UKE), 20251 Hamburg, Germany; [5]Department of Pharmacological and Biomolecular Sciences, Università degli Studi di Milano, 20133 Milan, Italy; [6]DFG Research Training Group 'Membrane Plasticity in Tissue Development and Remodeling', GRK 2213, Philipps-University of Marburg, 35032 Marburg, Germany. §current address: Institute of Chemistry and Biochemistry, Department of Biology, Chemistry and Pharmacy, Freie Universität Berlin, 14195 Berlin, Germany.

*__Correspondence to__

Marco B. Rust

Institute of Physiological Chemistry, Philipps-University of Marburg

35032 Marburg, Germany

Phone: +49-6421-2865020, E-Mail: rust@uni-marburg.de

Running title: CAP1 controls synaptic actin dynamics

Key words: CAP1; actin dynamics; dendritic spine; cofilin; cyclase-associated protein

Abstract

The vast majority of excitatory synapses are formed on small dendritic protrusions termed dendritic spines. Dendritic spines vary in size and density that are both crucial determinants of excitatory synaptic transmission. Aberrations in spine morphogenesis can compromise brain function and have been associated with neuropsychiatric disorders. Because actin filaments (F-actin) are the major structural component in spines, actin-binding proteins (ABP) that control F-actin dis-/assembly moved into the focus as critical regulators of brain function. Indeed, mouse studies identified the ABP cofilin1 as a key regulator of spine morphology, synaptic transmission and behavior. These studies emphasized the necessity for a tight control of cofilin1 to ensure proper brain function. We report spine enrichment of cyclase-associated protein 1 (CAP1), a conserved multidomain protein with largely unknown physiological functions. Super-resolution microscopy and live cell imaging of CAP1-deficient hippocampal neurons revealed impaired synaptic F-actin organization and dynamics associated with alterations in spine morphology. Mechanistically, we found that CAP1 cooperated with cofilin1 in spines and that its helical folded domain mediated this interaction. Moreover, our data proved functional interdependence of CAP1 and cofilin1 in control of spine morphology. In summary, we identified CAP1 as a novel regulator of the postsynaptic actin cytoskeleton that was essential for synaptic cofilin1 activity.

Introduction

Most excitatory synapses in the vertebrate brain are formed on small dendritic protrusions termed dendritic spines (Bosch, 2012). Dendritic spines are composed of specialized subdomains exerting specific functions in excitatory synaptic transmission. Their postsynaptic density (PSD) opposes the presynaptic active zone and contains neurotransmitter receptors, ion channels and signaling molecules that collectively mediate postsynaptic responses to neurotransmitter release (Sheng, 2007). These proteins are anchored via scaffolding molecules that connect the PSD to the underlying cytoskeleton. Actin filaments (F-actin) are the major cytoskeletal component in spines, and actin-binding proteins (ABP) that regulate assembly or disassembly of F-actin control spine morphology and density (Bosch, 2012). Consequently, dysfunction of ABPs causes aberrations in spine morphology or density that affect synaptic transmission and brain function and that have been associated with mental retardation or neuropsychiatric diseases such as autism spectrum disorders (ASD), attention-deficit/hyperactivity disorder (ADHD) or schizophrenia (Bourgeron, 2015; Hlushchenko, 2016; Spence, 2015). Hence, deciphering postsynaptic actin regulatory mechanisms is mandatory to understand the processes that control brain function and that contribute to pathologies of human neuropsychiatric diseases.

Studies of the past decade unraveled important synaptic functions for actin depolymerizing proteins of the ADF/cofilin family (Bosch, 2014; Duffney, 2015; Feuge, 2019; Goodson, 2012; Gu, 2010; Hotulainen, 2009; Pyronneau, 2017; Rust, 2010; Sungur, 2018; Wolf, 2015; Zimmermann, 2015). Specifically, these studies identified cofilin1 as a key regulator of postsynaptic F-actin dynamics, spine morphology, synapse physiology and brain function. Further, they implicated cofilin1 in the pathology of neuropsychiatric diseases and proved modulation of actin-regulatory mechanisms as a promising therapeutic avenue. Collectively, these studies highlighted the necessity for a tight regulation of cofilin1 activity to ensure synapse physiology (Ben Zablah, 2020; Rust, 2015a; Rust, 2015b). To date, various mechanisms that control synaptic cofilin1 have been identified, including signaling cascades that control cofilin1-actin interaction via posttranslational modifications, proteins that mediate cofilin1 recruitment into spines and local cofilin1 translation within the dendritic compartment (Feuge, 2019; Meng, 2002; Pelucchi, 2020; Pontrello, 2012; Rust, 2015a).

Cyclase-associated protein 1 (CAP1) is a highly conserved, multidomain protein ABP with largely unknown physiological functions (Rust, 2020). We found CAP1 enriched in spine heads underneath the PSD. Inactivation of CAP1 in primary hippocampal neurons from gene-targeted mice revealed a role for CAP1 in regulating the postsynaptic actin cytoskeleton as well as spine morphology and density. CAP1's function in regulating spine morphology and density depended on its helical-folded domain (HFD) that mediated interaction with cofilin1 in neurons. Rescue experiments in double knockout neurons lacking CAP1 and cofilin1 revealed their cooperation in the regulation of spine morphology and they proved functional interdependence of both ABP in the postsynaptic compartment. Together, we found CAP1 to be relevant for cofilin1 function in spines. We thereby report a novel mechanism that controls synaptic cofilin1 activity.

Results

CAP1 is enriched in dendritic spine heads, beneath the postsynaptic density

Previous studies reported presence of CAP1 during embryonic brain development (Bertling, 2004; Schneider, 2021a), but its expression in the postnatal brain and its subcellular localization in differentiated neurons is unknown. To determine CAP1 expression in the postnatal brain, we performed immunoblots with mouse cerebral cortex lysates at various postnatal stages. We found CAP1 present at postnatal day (P) 0 and increasing expression starting during the 2nd postnatal week (Fig. 1A). Similarly, CAP1 expression increased during the 2nd week in cultured mouse neurons suggesting that they imitated the temporal expression profile *in vivo* (Fig. 1B). Additionally, we determined whether CAP1 was present in synapse-enriched fractions termed synaptosomes. We separated synaptosomal lysates into soluble and insoluble protein fractions. Separation has been verified by immunoblotting against synaptophysin and PSD-95, respectively (Fig. 1C). We found CAP1 in the soluble, but not in the insoluble fraction. Together, CAP1 was expressed throughout postnatal mouse brain development with increasing expression levels during neuron differentiation, and our data suggested synaptic localization.

To further study the subcellular localization of CAP1, we exploited mouse hippocampal neurons isolated at embryonic day 18.5 (E18.5). We transfected neurons after 6 days *in vitro* (DIV) with constructs expressing green fluorescence protein-tagged CAP1 (CAP1-GFP) and the volume marker *Discosoma* red fluorescence protein (dsRed), and we determined CAP1-GFP localization at DIV16 (Fig. 1D). In control experiments, we expressed GFP that showed the expected equal distribution within the dendritic compartment as evident from a fluorescence intensity profile that overlapped with dsRed (Fig. 1E). We found CAP1-GFP present in virtually all dendritic spines, independent of their size or morphology (Fig. 1D). When compared to GFP-expressing control neurons, GFP intensity appeared stronger in spines from neurons expressing CAP1-GFP (Fig. 1D-F). Indeed, the ratio of GFP intensity in spine heads vs dendritic shafts was more than twofold increased in CAP1-GFP neurons when compared to GFP-expressing control neurons (Fig. 1G; GFP: 0.56±0.02, CAP1-GFP: 1.31±0.07, n=150 spines from 20 neurons from 3 hippocampal cultures, $P<0.001$), and the ratio in spine heads vs spine necks was increased by roughly 50% (GFP: 1.58±0.04, CAP1-

GFP: 2.40±0.10, n=150/20/3, P<0.001). These data suggested CAP1 enrichment in spine heads, which was further supported by co-localization of CAP1-GFP and the F-actin marker mCherry-LifeAct (Fig. S1A-B). CAP1 immunoreactivity confirmed CAP1 enrichment in spines, thereby proving that CAP1-GFP faithfully reflects localization of endogenous protein (Fig. S1C). Control experiments in hippocampal neurons from brain-specific CAP1-KO mice (Schneider, 2021a) confirmed specificity of the CAP1 antibody (Fig. S1D).

To determine the sub-synaptic localization of endogenous CAP1, we performed stimulated emission depletion (STED) nanoscopy. We confirmed CAP1 localization in spines and additionally found CAP1 in presynaptic boutons identified by Bassoon immunoreactivity (Fig. 1H). Fluorescent intensity profiles suggested abundance of CAP1 in spine regions beneath the Shank3-labelled PSD (Fig. 1I). To better characterize CAP1 distribution in spines, we performed STED nanoscopy on neurons stained with Shank3 and the F-actin marker phalloidin (Fig. 1J), both of which were used to outline spines. We determined relative fluorescence of CAP1, Shank3 and phalloidin by using a mask that subdivides spines into quadrants (Q), which each were composed of three equally sized segments (see mask in Fig. 1K), similar to a previous study (Mikhaylova, 2018). As expected, Shank3 was enriched in QIV, opposite to the spine neck, and phalloidin intensity was equally high in QI-III, but low in QIV (Fig. 1K). CAP1 was present in all four quadrants, but intensity was somewhat higher in QII and III. These data revealed CAP1 enrichment in spine heads outside the PSD and spine head base (Fig. 1K). We also determined the centers of mass within spines for all three fluorescent signals. As shown in scheme (Fig. 1K), the coordinate system's origin represents the center of the circular region of interest. As expected, this analysis revealed no differences between Shank3, phalloidin and CAP1 along the y-axis (Fig. 1L; Shank3: -1.86±2.41, phalloidin: -0.74±1.29, CAP1: -1.05±1.50, n=20/3; Shank3 vs CAP1: P=0.812, phalloidin vs CAP1: P=0.893, Shank3 vs phalloidin: P=0.730). CAP1's center of mass along the x-axis, which approximately reflected the PSD-spine neck axis, laid between Shank3 and phalloidin and differed from both (CAP1: -7.93±0.93, Shank3: -14.88±2.15, P<0.05, phalloidin: 0.11±1.44, P<0.001). These data confirmed CAP1 enrichment in spine head regions underneath the PSD. Together, our data revealed localization of endogenous CAP1 in both pre- and postsynaptic

compartments of hippocampal excitatory synapses and an enrichment in spine heads, beneath the PSD.

CAP1 was specifically relevant for dendritic spine density and morphology

To investigate the role of CAP1 in dendritic spines, we genetically removed CAP1 from isolated hippocampal neurons. Since systemic CAP1 mutant mice died during embryonic development (Jang, 2019), we exploited hippocampal neurons from conditional mice ($CAP1^{flx/flx}$) in which we flanked exon 3 of the CAP1 gene by loxP sites (Schneider, 2021a). We transfected isolated hippocampal neurons from E18.5 $CAP1^{flx/flx}$ mice with either catalytically active mCherry-tagged Cre (Cre) or with a catalytically inactive mCherry-Cre mutant (Cre-mut) at DIV6. Immunocytochemistry proved absence of CAP1 from Cre-transfected $CAP1^{flx/flx}$ neurons at DIV16 (Fig. S2), which we refer to as CAP1-KO throughout the manuscript. Instead, CAP1 was present upon Cre-mut transfection, and these neurons served as controls (CTR).

To characterize CAP1's neuronal function, we performed a thorough morphometric analysis of GFP-transfected neurons at DIV16 (Fig. 2A). In CAP1-KO neurons, the number of primary neurites, the number of branching points as well as the dendrite complexity deduced from the branching point number normalized to dendritic length was unchanged (Fig. S3A-C; primary neurites: CTR: 5.79±0.49, CAP1-KO: 6.04±0.53, n=15 neurons from 3 cultures, P=0.731; branching points: CTR: 50.50±7.02, CAP1-KO: 39.58±5.07, n=15/3, P=0.214; branching points/total length: CTR: 0.021±0.002, CAP1-KO: 0.024±0.003, n=15/3, P=0.293). We therefore concluded that CAP1 was dispensable for dendritic tree complexity.

The observed CAP1 enrichment in spines led us determine spine density and morphology. Compared to CTR, spine density was reduced by 17% in CAP1-KO neurons, while spine volume was increased by 27% (Fig. 2A-C; density (spines/µm): CTR: 0.47±0.03, CAP1-KO: 0.39±0.04, n>3,750/15/3, P<0.01; volume (arbitrary units (au)): CTR: 0.22±0.01, CAP1-KO: 0.28±0.03, n>3,750/15/3, P<0.001). Consistent with enlarged spine volume, spine head width was increased by 31%, while total spine length or spine head length were unchanged (Fig. 2D-F; (µm) spine length: CTR: 1.51±0.10, CAP1-KO: 1.42±0.09, P=0.488; head length: CTR: 0.93±0.08, CAP1-KO: 0.85±0.06, P=0.459; head width: CTR: 0.51±0.01, CAP1-KO: 0.67±0.03, P<0.001;

n>250/15/3). Further, we determined the fractions of spine types in CAP1-KO neurons (Fig. S3D), similar to previous studies (Hering, 2001). Compared to CTR, the fractions of filopodia-like and thin spines were reduced by 67% and 33%, respectively, in CAP1-KO neurons, while the fractions of stubby or mushroom-like spines were increased by 62% and 31%, respectively (Fig. 2G; filopodia-like: CTR: 0.08±0.02, CAP1-KO: 0.03±0.01, thin: CTR: 0.39±0.03, CAP1-KO: 0.27±0.03; stubby: CTR: 0.13±0.02, CAP1-KO: 0.22±0.03; mushroom-like: CTR: 0.29±0.02, CAP1-KO: 0.37±0.03; n>250/15/3). Consequently, the spine type distribution was altered in CAP1-KO neurons (P<0.001). Together, CAP1 inactivation did not impair neuron differentiation, but increased spine size and reduced spine density. Further, the spine type distribution was shifted towards mature spines (stubby, mushroom-like) in CAP1-KO neurons. Since F-actin constitutes the major structural component in spines and thereby determines spine morphology, we hypothesize a role for CAP1 in regulating the postsynaptic actin cytoskeleton.

CAP1 controls F-actin organization and actin turnover in spines

To test whether CAP1 regulates the postsynaptic actin cytoskeleton, we investigated both F-actin organization and actin dynamics in spines. For better comparability, we restricted our analysis to mushroom-like spines, which displayed a 22% increase in spine head width in CAP1-KO neurons (Figs. 3A; (µm) total length: CTR: 1.59±0.09, CAP1-KO: 1.69±0.11, P=0.510; head length: CTR: 0.69±0.05, CAP1-KO: 0.75±0.04, P=0.466; head width: CTR: 0.76±0.02, CAP1-KO: 0.93±0.05, P<0.01), while the morphologies of filopodia-like, thin or stubby spines were unchanged (Fig. S3E-G; filopodia-like: length: CTR: 2.91±0.15, CAP1-KO: 2.90±0.48, P=0.976; width: CTR: 0.27±0.01, CAP1-KO: 0.27±0.01, P=0.952; thin: total length: CTR: 1.28±0.05, CAP1-KO: 1.13±0.07, P=0.100; head length: CTR: 0.80±0.05, CAP1-KO: 0.79±0.05, P=0.933; head width: CTR: 0.36±0.01, CAP1-KO: 0.36±0.02, P=0.770; stubby: length: CTR: 0.50±0.02, CAP1-KO: 0.55±0.04, P=0.180; width: CTR: 0.51±0.05, CAP1-KO: 0.56±0.05, P=0.464; n>250/15/3). To study whether CAP1 was relevant for actin turnover in spines, we expressed GFP-actin in CTR and CAP1-KO neurons and performed fluorescent recovery after photobleaching (FRAP) experiments in individual spines (Fig. 3B, Movies S1-2). During 300 s of recording, GFP-actin levels in CTR neurons recovered and reached a plateau at roughly 80% of basal levels (Fig. 3C-D).

The stable actin fraction that did not recover within 300 s amounted to 0.22±0.02 (n=32/8/3), similar to previous studies (Feuge, 2019; Michaelsen-Preusse, 2016). While this fraction was 54% higher in CAP1-KO neurons (0.34±0.06, n=33/9/3), the increase did not reach statistical significance (P=0.087). However, compared to CTR, actin turnover was slower in spines from CAP1-KO neurons, as evident from a 51% increase in half-recovery time of the dynamic actin fraction (Fig. 3E; (s) CTR: 31.60±5.76, CAP1-KO: 47.75±4.83, P<0.05). Hence, actin turnover was slowed down in CAP1-KO spines, demonstrating a role for CAP1 in postsynaptic actin dynamics.

Next, we tested whether impaired actin dynamics were associated with an altered F-actin organization in spines. We therefore performed STED imaging on GFP-expressing neurons stained with phalloidin to label F-actin (Fig. 3F). GFP was used to outline spines and, thus, to determine distribution of fluorescence intensities of phalloidin as shown in the scheme in Fig. 1K. In CTR, we found the expected homogenous distribution of phalloidin in QI-III and lower levels in QIV (Fig. 3G). Compared to CTR, phalloidin distribution was different in CAP1-KO spines, in which it was enriched in QI, at the spine head base. Hence, F-actin organization was altered in spines of CAP1-KO neurons. Because the actin cytoskeleton is relevant for anchoring scaffolding proteins of the PSD, we next determined by STED nanoscopy whether disorganization of F-actin in CAP1-KO neurons was associated with an altered sub-spinous distribution of the key PSD proteins Shank3, PSD-95 and Homer (Fig. 3F). As expected, all three scaffolding proteins were enriched in QIV in CTR spines (Fig. 3G). Instead, such an enrichment was not present in spines from CAP1-KO neurons. We also determined the centers of mass for phalloidin, PSD-95, Shank3 and Homer in CTR and CAP1-KO spines (Fig. 3H). To exclude potential discrepancies due to differences in spine size and morphology between both groups, we normalized the centers of mass to that of GFP, which corresponded to the coordinate system's origin. Consistent with a homogenous distribution of phalloidin in QI-III from CTR spines, it's center of mass was close to the origin with a x-value of -1.65±1.63 (n=26). The centers of mass for PSD-95, Shank3 and Homer were found further on the left, as expected from their enrichment in QIV (x-values: PSD-95: -7.68±1.74, n=30; Shank3: -8.88±2.25, n=26; Homer: -8.11±1.38, n=57). Compared to CTR, the centers of mass were different for phalloidin and all three PSD proteins in CAP1-KO spines, thereby confirming F-actin disorganization in these spines and an altered localization of

postsynaptic proteins (x-values: phalloidin: 3.91±2.00, P<0.05, n=29; PSD-95: -1.64±2.16, P<0.05, n=24; Shank3: 0.89±2.99, P<0.05, n=29; Homer: -2.18±1.72, P<0.001, n=47). Hence, our data revealed an altered F-actin distribution within CAP1-KO spines, demonstrating a role for CAP1 in organizing the postsynaptic actin cytoskeleton. Interestingly, F-actin disorganization was associated with an altered distribution of key PSD proteins. Together, we identified CAP1 as a novel regulator of the postsynaptic actin cytoskeleton relevant for both actin dynamics and F-actin organization.

CAP1 domains mediating ADF/cofilin interaction are relevant for its function in spines

Having established CAP1 as a novel regulator of the postsynaptic actin cytoskeleton relevant for spine density and morphology, we next set out to determine the CAP1-dependent mechanism. CAP1 is a multi-domain protein comprising several conserved domains capable of binding both actin as well as ABPs (Rust, 2020). By exploiting recombinant proteins and mutant yeast strains, recent studies implicated its helical folded domain (HFD) as well as β-sheets within its CARP domain in actin dynamics, and they identified amino acid residues essential for these activities (Kotila, 2018; Kotila, 2019). To test whether HFD and/or CARP domain were relevant in spines, we expressed myc-tagged mutant CAP1 variants (CAP1-HFD and CAP1-CARP, respectively) in CAP1-KO neurons (Fig. 4A). These experiments also included a CAP1 variant with mutations in a proline-rich domain (CAP1-P1) that reportedly disrupted interaction with the ABP profilin (Bertling, 2007; Makkonen, 2013), an important regulator of spine morphology (Ackermann, 2003; Lamprecht, 2006; Michaelsen-Preusse, 2016; Michaelsen, 2010). In control experiments, we expressed myc-tagged WT-CAP1 in hippocampal neurons. Myc antibody staining confirmed localization of WT-CAP1 and all three CAP1 mutants in spines from CTR and CAP1-KO neurons (Fig. 4B). Spines were identified by co-transfection of GFP that served as volume marker. WT-CAP1 did not alter spine density and only very slightly reduced spine volume in CTR neurons, while CAP1 mutants neither altered spine density nor volume in CTR neurons (Fig. 4C-D; density (spines/µm): CTR: 0.47±0.03; WT-CAP1: 0.46±0.03, P=0.613; CAP1-HFD: 0.46±0.05, P=0.602; CAP1-CARP: 0.47±0.03, P=0.860; CAP1-P1: 0.48±0.03, P=0.857; n>3,750/15/3 for each condition; volume

(a.u.): CTR: 0.22±0.01; WT-CAP1: 0.20±0.01, P<0.05; CAP1-HFD: 0.21±0.02, P=0.372; CAP1-CARP: 0.24±0.01, P=0.175; CAP1-P1: 0.22±0.02, P=0.705; n>3,750/15/3 for each condition). In contrast, WT-CAP1 increased spine density by 20% in CAP1-KO neurons, and it reduced spine volume by 22% (density (spines/µm): CAP1-KO: 0.39±0.04, WT-CAP1: 0.47±0.05, P<0.05, n>3,750/15/3; volume (a.u.): CAP1-KO: 0.28±0.03, WT-CAP1: 0.22±0.02, P<0.01, n>3,750/15/3). Consequently, spine density and volume in WT-CAP1-expressing CAP1-KO neurons were not different from CTR neurons (P=0.993 and P=0.825, respectively). Hence, re-expression of WT-CAP1 fully rescued spine morphological changes in CAP1-KO neurons. Similarly, CAP1-P1 rescued spine changes in CAP1-KO neurons (density (spines/µm): 0.48±0.04, P<0.05, n>3,750/15/3; volume (a.u.): 0.22±0.02, P<0.01, n>3,750/15/3). Instead, neither CAP1-HFD nor CAP1-CARP changed spine density or volume in CAP1-KO neurons (density (spines/µm): CAP1-HFD: 0.38±0.03, P=0.837; CAP1-CARP: 0.42±0.03, P=0.349; n>3,750/15/3; volume (a.u.): CAP1-HFD: 0.27±0.02, P=0.684; CAP1-CARP: 0.27±0.02 P=0.497; n>3,750/15/3). We therefore concluded that HFD and CARP domain of CAP1, but not the P1 domain, are relevant for spine morphology. In a current model for CAP1-dependent regulation of actin dynamics, HFD mediates interaction with F-actin-bound ADF/cofilin and thereby promotes dissociation of terminal actin subunits. Subsequently, CARP domain releases ADF/cofilin from the G-actin complex (Kotila, 2018; Kotila, 2019; Rust, 2020). Hence, our rescue experiments in CAP1-KO neurons let us hypothesize an interaction of CAP1 and ADF/cofilin in spines.

CAP1 and cofilin1 physically interact in hippocampal homogenates and neurons

The ADF/cofilin family comprises cofilin1, cofilin2 and actin depolymerizing factor (ADF, also known as destrin). While all three family members are expressed in the mouse brain (Bellenchi, 2007; Gurniak, 2014), only cofilin1 and ADF have been localized in excitatory synapses, and cofilin1 emerged as the key ADF/cofilin protein in synaptic actin dynamics and spine morphology (Bosch, 2014; Görlich, 2011; Herde, 2010; Hotulainen, 2009; Racz, 2006; Rust, 2015a; Rust, 2010). Based on these reports, we tested whether CAP1 interacts with cofilin1 in spines. Fluorescent intensity profiles in neurons overexpressing CAP1-mCherry and cofilin1-GFP suggested co-localization of both actin regulators in dendritic spines (Fig. 5A-B). Indeed, proximity

ligation assays exploiting antibodies against CAP1 and cofilin1 confirmed co-localization of endogenous proteins in the dendritic compartment including dendritic spines (Fig. 5C). By co-immunoprecipitation (CoIP), we further tested for physical interaction between CAP1 and cofilin1. To do so, we coupled a mouse monoclonal antibody against CAP1 to magnetic beads, which we incubated with mouse hippocampal homogenate. Immunoblot analysis revealed presence of both CAP1 (identified by exploiting a rabbit polyclonal antibody) and cofilin1 in precipitated complexes, thereby demonstrating physical interaction of both actin regulators in hippocampus (Fig. 5D). We confirmed their physical interaction in a mouse hippocampal neuronal cell line. In these experiments, we overexpressed myc-WT-CAP1 together with either GFP or GFP-WT-cofilin1 in HT-22 cells. Myc-WT-CAP1 was precipitated with an antibody against GFP in HT-22 cells overexpressing myc-WT-CAP1 together with GFP-WT-cofilin1, but not in HT-22 cells overexpressing myc-WT-CAP1 together with GFP (Fig. 5E-F). We also overexpressed GFP-WT-cofilin1 together with the CAP1 mutant variant myc-CAP1-HFD that was not able to rescue spine morphology in CAP1-KO neurons (Fig. 4B-D). Interestingly, hardly any myc-CAP1-HFD was precipitated with an antibody against GFP in these cells (Fig. 5E-F), confirming that CAP1's HFD is relevant for the interaction with cofilin1 (Kotila, 2018; Kotila, 2019). Together, co-localization of CAP1 and cofilin1 in spines as well as their physical interaction in hippocampal neurons strengthened our hypothesis that both actin regulators cooperate in regulating spine morphology.

Cofilin1-KO neurons display spine changes similar to CAP1-KO neurons

To test this hypothesis, we chose a genetic approach and compared under identical experimental conditions spine defects in CAP1-KO neurons to those in neurons lacking either cofilin1 alone or together with CAP1. We generated cofilin1-KO neurons by Cre expression in hippocampal neurons from E18.5 $Cfl1^{flx/flx}$ mice (Bellenchi, 2007), $Cfl1^{flx/flx}$ mice neurons expressing Cre-mut served as CTR (Fig. 6A). Cofilin1-KO neurons displayed increased spine density and volume (Fig. 6B-C; density (spines/µm): CTR: 0.38±0.01, cofilin1-KO: 0.44±0.01, n>3,750/15/3, P<0.001; volume (a.u.): CTR: 0.23±0.01, cofilin1-KO: 0.32±0.01, n>3,750/15/3, P<0.001), similar to spine changes reported for cofilin1-KO mice (Rust, 2010). Further analysis of cofilin1-KO neurons showed a 20% increase in spine head width, while total spine length or

spine head length were unchanged, similar to CAP1-KO neurons (Fig. 6D-F; (µm) spine length: CTR: 1.42±0.08, cofilin1-KO: 1.46±0.05, P=0.643; head length: CTR: 0.89±0.04, cofilin1-KO: 0.80±0.03, P=0.130; head width: CTR: 0.59±0.02, cofilin1-KO: 0.71±0.02, P<0.001; n>250/15/3). While morphometric analysis of individual spine types did not reveal differences between CTR and cofilin1-KO neurons (Fig. S4A-D; (µm) mushroom-like: total length: CTR: 1.55±0.07, cofilin1-KO: 1.70±0.04, P=0.085; head length: CTR: 0.61±0.02, cofilin1-KO: 0.67±0.02, P=0.097; head width: CTR: 0.85±0.04, cofilin1-KO: 0.93±0.02, P=0.059; filopodia-like: length: CTR: 3.07±0.17, cofilin1-KO: 3.13±0.22, P=0.819; width: CTR: 0.19±0.01, cofilin1-KO: 0.25±0.02, P=0.086; thin: total length: CTR: 1.36±0.06, cofilin1-KO: 1.26±0.04, P=0.190; head length: CTR: 0.91±0.05, cofilin1-KO: 0.84±0.05, P=0.307; head width: CTR: 0.31±0.01, cofilin1-KO: 0.32±0.02, P=0.610; stubby: length: CTR: 0.54±0.04, cofilin1-KO: 0.54±0.03, P=0.944; width: CTR: 0.71±0.05, cofilin1-KO: 0.71±0.03, P=0.972; n>250/15/3), the spine distribution among different categories was altered in cofilin1-KO neurons (Fig. 6G; n>300/15/3, P<0.01). Specifically, the fractions of filopodia-like (-57%) and thin spines (-29%) were reduced, while the fractions of stubby (+45%) and mushroom-like spines (+25%) were increased (filopodia-like: CTR: 0.07±0.01, cofilin1-KO: 0.04±0.01, thin: CTR: 0.35±0.03, cofilin1-KO: 0.25±0.02; stubby: CTR: 0.11±0.02, cofilin1-KO: 0.16±0.01; mushroom-like: CTR: 0.40±0.05, cofilin1-KO: 0.50±0.02; branched: CTR: 0.04±0.01, cofilin1-KO: 0.02±0.01; n>250/15/3). Hence, the spine type distribution in cofilin1-KO neurons was shifted towards mature spines (P<0.01). Together, cofilin1-KO neurons displayed an increase in spine volume and spine head width as well as a shift in the spine type distribution towards mature spines, similar to CAP1-KO neurons.

CAP1 and cofilin1 cannot compensate each other's inactivation

The primary function of cofilin1 is to dynamize F-actin by accelerating the dissociation of actin subunits (Hild, 2014). Consequently, cofilin1 inactivation stabilizes F-actin, thereby causing an increase in spine size (Rust, 2010; Wolf, 2015; Zimmermann, 2015). Since we found a similar function for CAP1 in spines and similar changes in spine morphology in CAP1-KO neurons, we next tested whether CAP1 or cofilin1 were able to compensate each other's inactivation. To do so, we overexpressed WT-cofilin1 in CAP1-KO neurons at DIV6 and, *vice versa,* WT-CAP1 in cofilin1-KO neurons.

Overexpression of WT-cofilin1 neither altered spine density nor volume in CAP1-KO neurons at DIV16 (Fig. 7A-C; density (spines/µm): CTR: 0.42±0.02, CTR+WT-cofilin1: 0.45±0.02, P=0.399; CAP1-KO: 0.34±0.02, CAP1-KO+WT-cofilin1: 0.32±0.03, P=0.512, n>3,750/15/3 for each condition; volume (a.u.): CTR: 0.21±0.01, CTR+WT-cofilin1: 0.19±0.01, P=0.311; CAP1-KO: 0.27±0.01, CAP1-KO+WT-cofilin1: 0.28±0.01, P=0.713; n>3,750/15/3 for each condition). Upon WT-cofilin1 overexpression, spine density and volume were both still different between CAP1-KO and CTR (P<0.001 for density and volume). Likewise, WT-CAP1 overexpression did not alter spine density or volume in cofilin1-KO neurons at DIV16 (Fig. 7D-F; density (spines/µm): CTR: 0.40±0.01, CTR+WT-CAP1: 0.40±0.01, P=0.880; cofilin1-KO: 0.47±0.01, cofilin1-KO+WT-CAP1: 0.47±0.01, P=0.945; n>3,750/15/3 for each condition; volume (a.u.): CTR: 0.20±0.01, CTR+WT-CAP1: 0.21±0.01, P=0.748; cofilin1-KO: 0.27±0.01, cofilin1-KO+WT-CAP1: 0.26±0.01, P=0.166; n>3,750/15/3 for each condition). Both parameters were still increased in WT-CAP1-overexpressing cofilin1-KO neurons when compared to CTR neurons (P<0.001 for density and volume). Together, overexpression of either WT-CAP1 or WT-cofilin1 failed in rescuing spine defects in neurons lacking cofilin1 or CAP1, respectively. We therefore concluded that cofilin1 and CAP1 were not able to compensate each other's inactivation in spines.

CAP1 and cofilin1 are functionally interdependent in spines

Next, we set out to test whether CAP1 and cofilin1 cooperated in spines or controlled spine morphology via independent pathways. We therefore analyzed double KO (dKO) neurons with compound inactivation of CAP1 and cofilin1, which we achieved by Cre expression in CAP1$^{flx/flx}$/Cfl1$^{flx/flx}$ neurons. CAP1$^{flx/flx}$/Cfl1$^{flx/flx}$ neurons expressing Cre-mut served as CTR (Fig. 8A). Different from CAP1-KO or cofilin1-KO neurons, spine density was only very slightly reduced in dKO neurons (Fig. 8B; density (spines/µm): CTR: 0.39±0.01, dKO: 0.36±0.01, n>3,750/15/3, P<0.05). However, spine volume was increased by roughly 40% (Fig. 8C; volume (a.u.): CTR: 0.21±0.01, dKO: 0.30±0.01, n>3,750/15/3, P<0.001). Notably, spine volume in dKO neurons did not differ from CAP1-KO (P=0.136) or cofilin1-KO neurons (P=0.143). Hence, compound inactivation of CAP1 and cofilin1 did not cause an additive effect in spine volume.

A detailed spine morphometric analysis in dKO neurons revealed a 40% increase in spine head width, while total spine length or spine head length were unchanged (Fig. 8D-F; (µm) spine length: CTR: 1.62±0.08, dKO: 1.56±0.07, P=0.553; head length: CTR: 1.03±0.08, dKO: 0.91±0.05, P=0.209; head width: CTR: 0.60±0.03, dKO: 0.87±0.05, P<0.001; n>250/15/3). While morphology of filopodia-like and stubby spines was normal in dKO (Fig. S5A-D; (µm) filopodia-like: length: CTR: 3.10±0.19, dKO: 3.03±0.12, P=0.787; width: CTR: 0.28±0.02, dKO: 0.32±0.04, P=0.371; stubby: length: CTR: 0.64±0.05, dKO: 0.63±0.05, P=0.943; width: CTR: 0.77±0.07, dKO: 0.93±0.10, P=0.242, n>300/15/3), total length was reduced by 15% in thin spines and head width was increased by 20% in mushroom-like spines ((µm) thin: total length: CTR: 1.41±0.06, dKO: 1.21±0.08, P<0.05; head length: CTR: 0.84±0.08, dKO: 0.79±0.07, P=0.607; head width: CTR: 0.35±0.03, dKO: 0.35±0.03, P=0.919; mushroom-like: total length: CTR: 1.75±0.12, dKO: 1.82±0.07, P=0.649; head length: CTR: 0.73±0.05, dKO: 0.82±0.03, P=0.105; head width: CTR: 0.92±0.06, dKO: 1.12±0.05, P<0.05). Spine categorization according to their morphology revealed reduced fractions of filopodia-like (-50%) and thin spines (-45%) and increased fractions of stubby (+50%) and mushroom-like spines (+60%; Fig. 8G; filopodia-like: CTR: 0.10±0.01, dKO: 0.05±0.01; thin: CTR: 0.38±0.03, dKO: 0.21±0.02; stubby: CTR: 0.12±0.02, dKO: 0.18±0.02; mushroom-like: CTR: 0.32±0.03, dKO: 0.51±0.02; branched: CTR: 0.06±0.02, dKO: 0.04±0.01; P<0.001, n>250/15/3). Hence, spine type distribution in dKO neurons was shifted towards mature spines. Together, spine size was increased in dKO neurons, and this enlargement was caused by thicker mushroom-like spines and by an increased fraction of mature spines. These changes were very similar to those we found in CAP1-KO and cofilin1-KO neurons, suggesting that both ABP cooperated in spines.

To finally test this, we expressed either WT-CAP1, WT-cofilin1 or both ABP in dKO neurons and determined spine volume as a readout. Neither WT-CAP1 nor WT-cofilin1 reduced spine volume in dKO neurons (Fig. 8H; (a.u.): dKO: 0.30±0.01, dKO+WT-CAP1: 0.30±0.01, P=0.749; dKO+WT-cofilin1: 0.30±0.01, P=0.781; n>3,750/15/3 for each condition). Compared to CTR, spine volume was still higher in dKO neurons expressing either WT-CAP1 or WT-cofilin1 (P<0.001 for both). Instead, spine volume was reduced in dKO neurons upon expression of WT-CAP1 together with WT-cofilin1 (0.24±0.01, n>3,750/15/3, P<0.001), and spine volume in these neurons was not

different from CTR (P=0.227). We also expressed WT-cofilin1 together with aforementioned CAP1 mutants in dKO neurons and found that spine volume was rescued upon expression of WT-cofilin1 together with CAP1-P1 (0.22±0.01, n>3,750/15/3, P<0.001). Spine volume in these neurons was not different from CTR (P=0.409). While expression of WT-cofilin1 together with CAP1-CARP slightly reduced spine volume in dKO neurons (0.26±0.01, n>3,750/15/3, P<0.05), it did not change spine volume upon co-expression with CAP1-HFD (0.28±0.01, n>3,750/15/3, P=0.187). In dKO neurons expressing WT-cofilin1 together with either CAP1-HFD or CAP1-CARP, spine volume was still higher when compared to CTR (P<0.001). In summary, these data demonstrated that CAP1 and cofilin1 cooperated in the regulation of spine size. Further, they revealed functional interdependence of CAP1 and cofilin1 in spines.

Discussion

The ABP CAP1 is a multidomain protein with largely unknown physiological functions. In this study, we found increasing CAP1 expression during neuron maturation and an enrichment in dendritic spines. By STED nanoscopy and live cell imaging in hippocampal neurons from gene-targeted mice, we identified CAP1 as a novel regulator of the postsynaptic actin cytoskeleton that controls spine density and morphology. Mechanistically, we found CAP1's HFD to be relevant for its function in spines. Further, we showed that HFD mediates interaction with the key actin regulator cofilin1 and that both ABP cooperate in regulating spine morphology. Finally, rescue experiments in dKO neurons lacking CAP1 and cofilin1 demonstrated mutual functional dependence of both actin regulators in spines.

The yeast CAP ortholog has been recognized as an ABP three decades ago (for review: Ono, 2013; Rust, 2020), but significant progress in its molecular functions has been achieved only recently, predominantly by exploiting recombinant proteins or mutant yeast strains (Jansen, 2014; Johnston, 2015; Kotila, 2018; Kotila, 2019; Shekhar, 2019). In a current model of actin regulation, CAP interacts with cofilin-decorated F-actin via its HFD and thereby accelerates dissociation of the terminal actin subunit (Kotila et al., 2018, Kotila et al., 2019). Subsequently, G-actin-cofilin complexes are passed on to CAP's CARP domain that, together with its WH2 domain, releases cofilin from this complex and promotes nucleotide (ATP for ADP) exchange on G-actin, which is required for actin polymerization. While these studies provided exciting novel insights into CAP's molecular activities, the cellular and physiological functions of mammalian orthologs largely remained unknown, also because appropriate animal models were lacking. This held true specifically for CAP1, while earlier mouse studies implicated CAP2 in heart physiology and skeletal muscle development (Kepser, 2019; Colpan, 2021; Field, 2015; Peche, 2012). Recently, a TALEN-engineered systemic CAP1-KO mouse model has been generated, but these mice died during embryonic development and analysis of heterozygous mutants solely revealed a role for CAP1 in lipoprotein metabolism (Jang, 2019). By exploiting a conditional CAP1 strain and transgenic mice expressing Cre recombinase in neural stem cells under control of the nestin promoter, we have generated a brain-specific CAP1-KO mouse model (Schneider, 2021a; Tronche, 1999). Histology on CAP1-KO mice combined with an analysis of hippocampal neurons from these mutants revealed a role for CAP1 in

regulating actin dynamics relevant for growth cone morphology and motility, neuron differentiation as well as neuron connectivity (Schneider, 2021a; Schneider, 2021c). Instead, the function of CAP1 in differentiated neurons or synapses has not been studied to date.

In the present study, we demonstrated an important function for CAP1 in postsynaptic actin regulation, in good agreement with the molecular function identified in the above outlined *in vitro* and yeast studies. We here report CAP1 to be relevant for actin dynamics in spines and we earlier showed its relevance for actin dynamics in growth cones (Schneider, 2021a; Schneider, 2021c). We therefore postulate a general requirement for CAP1 in actin regulation both during neuron differentiation and in differentiated neurons, similar to cofilin1 (Bellenchi, 2007; Gomez, 2014; Omotade, 2017; Rust, 2015a; Rust, 2010; Schneider, 2021b). By PLA we found co-localization (within 40 nm) of CAP1 and cofilin1 in spines, and our CoIP validated their physical interaction in the hippocampus, which depended on CAP1's HFD. By rescue experiments in dKO neurons lacking CAP1 and cofilin1, we demonstrated a cooperation of both ABP in regulating spine morphology. Moreover, we showed mutual functional dependence of CAP1 and cofilin1 in spines, similar to their functional interdependence in growth cones (Schneider, 2021a).

While the present study for the first time reported an important synaptic function for CAP1, studies of the past two decades recognized cofilin1 as an important regulator of synapse physiology, brain function and behavior (Bosch, 2014; Fukazawa, 2003; Gu, 2010; Hotulainen, 2009; Rust, 2015b; Rust, 2010; Rust, 2015c; Zhou, 2004). In line with these studies, we found increased spine volume and density upon cofilin1 inactivation in primary hippocampal neurons. Collectively, these studies let cofilin1 emerge as a key regulator of spine morphology and as a major final point of signaling output for actin dynamics in spines (Spence, 2015). This emphasized the necessity for regulatory mechanisms that tightly control cofilin1 activity to ensure synapse physiology and brain function. In fact, dysregulation of cofilin1 activity has been linked to synaptic and behavioral deficits associated with ASD or ADHD (Duffney, 2015; Zimmermann, 2015). To date, a plethora of signaling molecules ranging from the Rho GTPases Rac1, Cdc42 and RhoA and their effectors PAK1, ROCK and LIMK1 to the phosphatase calcineurin and its effectors PI3K and slingshot have been implicated in synaptic cofilin1 phosphorylation that controls actin binding (for review: Ben Zablah,

2020; Rust, 2015b; Spence, 2015). Additionally, synaptic cofilin1 activity is regulated by molecules that control its recruitment into spines and by translation within the dendritic compartment (Feuge, 2019; Pelucchi, 2020; Pontrello, 2012). By demonstrating mutual functional dependence of cofilin1 and CAP1 in spines, we unraveled a conceptually novel mechanism of synaptic cofilin1 regulation. Further, our finding that CAP1 was essential for cofilin1 activity in spines opened up a new avenue for the modulation of synaptic cofilin1 activity and, hence, of synaptic actin dynamics. Notably, CAP1 comprises several conserved domains allowing interaction with molecules others than actin and cofilin1. To date, a number of interaction partners have been found for CAP1 or its homologs (for review: Kakurina, 2018; Ono, 2013; Rust, 2020), including established regulators of spine morphology such as the ABP profilin (Ackermann, 2003; Lamprecht, 2006; Michaelsen-Preusse, 2016; Michaelsen, 2010), the proteinase MMP-9 (Tian, 2007; Wang, 2008), the tyrosine kinases Abl1 and Abl2 (Lin, 2013; Ma, 2014; Omar, 2017), focal adhesion kinase (Moeller, 2006; Shi, 2009) and glycogen synthase kinase 3 (Ochs, 2015; Peineau, 2007). Normalization of spine parameters in CAP1-KO neurons upon expression of a CAP1 variant with a mutated proline-rich motif (CAP1-P1) suggested that its proline-rich domain and, hence, its interaction with profilin, were not relevant in spines. Nevertheless, it will be exciting to test in future studies whether other proteins interact with CAP1 in spines and how these proteins control synaptic CAP1-cofilin1 interaction, synaptic actin dynamics and spine morphology.

Apart from CAP1, mammals express a second family member, CAP2, with restricted expression pattern and abundance in striated muscles and brain (Rust, 2020). Similar to CAP1, CAP2 is expressed in the postnatal brain and located in spine heads from cortical and hippocampal neurons (Kumar, 2016; Pelucchi, 2020). However, while studies in mutant mice established important CAP2 functions in heart physiology and skeletal muscle development (Colpan, 2021; Field, 2015; Kepser, 2019; Peche, 2012), neuronal CAP2 functions are less clear. Increased spine density has been reported for cerebral cortex neurons, but this study unfortunately lacked a detailed spine morphometric analysis and did not provide mechanistic insights into spine density changes (Kumar, 2016). Conversely, spine density was unchanged upon shRNA-mediated CAP2 knockdown (CAP2-KD) in hippocampal neurons, and spine length and width were both slightly increased (Pelucchi, 2020). However, compared to 30%

increased spine size in CAP1-KO neurons, the effect of CAP2-KD on spine morphology was rather mild, suggesting that CAP1 is the key family member in spines. Instead, CAP2 seems to be more relevant than CAP1 for dendritic branching, because CAP2-KD, but not CAP1-KO, decreased dendritic length and arborization complexity. Interestingly, this study revealed CAP2-dependent cofilin1 recruitment into spines upon induction of long-term potentiation, which depended on disulfide bond-mediated CAP2 dimerization (Pelucchi, 2020). Although spine changes in CAP2-KD neurons suggested a role for CAP2 in synaptic actin dynamics, this has not been directly tested in this study. Moreover, it remained unknown whether CAP2 and cofilin1 cooperated in spine morphology and whether CAP2 was essential for synaptic cofilin1 activity as both shown in the present study for CAP1. Nevertheless, a model in which both CAP1 and CAP2 cooperate with cofilin1 in synaptic actin dynamics and spine morphology is very appealing, and it will be exciting in future studies to dissect CAP1- vs CAP2-specific mechanisms and to test whether or not CAP1 and CAP2 cooperate and/or are functionally redundant in spines.

In summary, we here identified CAP1 as an essential novel actin regulator in excitatory synapses that was relevant for organization and dynamics of postsynaptic F-actin and thereby controls spine density and morphology. Mechanistically, our data revealed mutual functional dependence of CAP1 and cofilin1 in spine morphology, thereby unravelling a novel actin regulatory mechanism in spines. Our data let us hypothesize that CAP1 is equally important as cofilin1 for brain function and behavior and that CAP1 dysregulation may contribute to the pathologies of neuropsychiatric disorders as it has been shown for cofilin1 (Duffney, 2015; Zimmermann, 2015).

Material and methods

Transgenic mice

Mice were housed in the animal facility of the University of Marburg on 12-hour dark-light cycles with food and water available *ad libitum*. Treatment of mice was in accordance with the German law for conducting animal experiments and followed the guidelines for the care and use of laboratory animals of the U.S. National Institutes of Health. Killing of mice has been approved by internal animal welfare authorities. Generation of CAP1$^{flx/flx}$ and Cfl1$^{flx/flx}$ mice have been described before (Bellenchi, 2007; Schneider, 2021a).

Cell culture and transfection

Primary hippocampal neurons from embryonic day 18.5 (E18.5) mice were prepared as previously described (Schratt, 2006). Briefly, hippocampi were dissociated, and neurons were plated at a density of 62,000/cm^2 on 0.1 mg/ml poly-L-lysine-coated coverslips. Neurons were cultured in Neurobasal medium containing 2% B27, 1 mM GlutaMax, 100 µg/ml streptomycin, and 100 U/ml penicillin (Gibco, Thermo Fischer) in a humidified incubator at 37°C with 5% CO_2. Neurons were transfected at DIV6 with 1 µg plasmid/well of 24 well plates using Lipofectamine 2000 reagent (Thermo Fischer) according to manufacturer's protocol.

HT-22 cells were plated at a density of 10,000 cells/cm^2 in cell culture dishes. 24 to 30 h after plating, HT-22 cells were transfected with 20 µg plasmid/dish using Lipofectamine 2000 reagent (Thermo Fischer). Cell culture medium was changed once roughly 20 h after transfection. 40 to 48 h later, HT-22 cells were harvested by scraping and homogenized in 1,500 µL lysis buffer (50 mM Tris/HCl pH 7.5, 150 mM NaCl, 1% Triton-X, Roche Proteinase inhibitors) using a dounce homogenizer. HT-22 lysates were then left on ice for approximately 30 min before centrifugation. The supernatant of each condition was collected and used for further analysis.

CAP1-eGFP overexpression plasmid-pcDNA3.1-CAP1-eGFP was purchased from Genscript. Other overexpression constructs, such as pEGFP-C1-CAP1, pmCherry-C1-CAP1 and pCMV-Myc-N-CAP1 were generated by amplification of CAP1 ORF from pcDNA3.1-CAP1-eGFP plasmid and cloning it in frame between corresponding restriction sites. Point mutations were introduced according to modified site-directed

mutagenesis protocol (Liu, 2008) by exploiting restriction sites and oligonucleotides as listed in Tab. S1.

Immunocytochemistry

Neurons were washed once with phosphate-buffered saline (PBS), fixed in 4% paraformaldehyde (PFA)/sucrose in PBS for 15 min and rinsed in PBS three times. After 10 min incubation in carrier solution (CS; 0.1% gelatin, 0.3% Triton-X100 in PBS), neurons were incubated with primary antibodies in CS for 2h. Thereafter, neurons were washed with PBS three times for 5 min and incubated with secondary antibodies in CS for 45 min. After washing five times with PBS, coverslips were mounted onto microscopy slides using AquaPoly/mount (Polysciences Inc.). Second last washing step included Hoechst if used.

For STED microscopy, neurons were incubated with permeabilization buffer (0.2% Triton-X-100 in PBS) for 10 min after fixation and washing with PBS. Subsequently, neurons were washed twice with PBS for 5 min and incubated with blocking buffer (BB, 10% horse serum with 0.1% Triton-X-100 in PBS) for 45-60 min. Thereafter, neurons were incubated with primary antibodies in BB o/n at 4°C. After three 10 min PBS washing steps, neurons were incubated with secondary antibodies in BB for 1h and washed with PBS five times for 10 min. In case phalloidin was included, neurons were incubated with phalloidin-Atto647N in PBS o/n at 4°C. Coverslips were mounted onto microscopy slides with Mowiol-488 mounting medium (ROTH, prepared according to manufacturer's instructions). Tab. S2-3 provide lists of primary and secondary antibodies, respectively, including Hoechst and phalloidin.

Dendrite morphology

Images were acquired with Zeiss LSM 5 PASCAL and PASCAL LSM5 software from a single optical plane with a 20x objective at a resolution of 1024x1024 pixels. Background of images were removed using the ImageJ extension program FIJI (https://fiji.sc). Dendrite morphology was assessed by using NeuroMath (version 3.4.8; (Rishal, 2013) and applying the following settings: noise level: 1, measure type: cell morphology, segmentation type: threshold, min. cell intensity: 50, min. area: 100, max. area: 600, min. diameter: 5, max. axial ratio: 10, min. neurite length: 32. Neurons of three independent biological replicates, each with eight images per condition were analyzed.

Spine analysis

Images were acquired with Leica TCS SP5 II LSM and LAS AF software using a 63x oil immersion objective. Images were acquired with a resolution of 2048x2048 or 1024x1024 pixels as z-stacks of 9 optical planes with a step size of 0.49 µm and projected to a single-plane image (maximum projection). To quantify spine density, individual spines were tagged with a circle of 2.254 µm² (FIJI 'oval' tool). Spine number was normalized to the length of the analyzed dendrite determined by using 'freehand line' tool. Spine volume was determined simultaneously by measuring mean signal intensity in the aforementioned circle. Usually 250-300 spines were counted per neuron from secondary and tertiary basal dendrites. For every neuron, the mean signal intensity of all analyzed spines was calculated and normalized to mean signal intensity of the respective dendritic shafts. Neurons of three independent biological replicates were analyzed, each with 5 neurons per condition. Spine morphology (total length, spine head length and width) was analyzed by using FIJI 'freehand selection' tool in images of dendrite sections with a length of approximately 30 µm. Based on these values, spines were categorized as shown in scheme in Fig. S3D. Spines that did not fit into these categories were classified as 'other'. The number of spines was normalized to the length of the respective dendrite. Neurons of three independent biological replicates were analyzed, each with 5 neurons per condition. Intensity profiles in confocal images were acquired with FIJI 'plot profile' tool. Lines were selected in a way that they cover two spines and interjacent dendritic shaft. GFP ratios between spine head vs dendritic shaft or vs spine neck were analyzed with 'freehand selection' tool. Like this, mean signal intensities in spine head, spine neck or an underlying piece of dendrite was determined, which were used to calculate the ratios of mean signal intensities.

FRAP analysis

Hippocampal neurons were cultured on 35 mm glass bottom dishes (WillCo-dish®) coated with poly-L lysine, transfected at DIV7 with pEGFP-C1-Actin and pCig2-CRE-mCherry or pCig2-CRE-mut-mCherry plasmids. The FRAP imaging was carried out with Leica TCS SP5 II (FRAP-Wizard) equipped with a temperature-controlled chamber. DIV16-17 neurons were imaged with 63x objective at 35°C in 1xHBSS (Gibco; supplemented with 4 mM $NaCO_3$ and 2 mM $CaCl_2$). The following imaging settings were applied: format 512x512 pixel, speed 700 Hz, 2-line averaging, pinhole

300 µm, 15% of argon laser power, bleaching with 100 % and image acquisition with 3-7% power intensity of AOTF 488 nM (FRAP-wizard). Imaging/bleaching program: prebleaching 5x 2 s, bleaching 5x 1,5 s (3 µm diameter), postbleaching 20x 2 s, 10x 5 s and 20x 10 s.

The image series were analysed using FIJI as previously reported (Michaelsen-Preusse, 2016). Briefly, background and bleaching correction was applied and normalized fluorescence intensity for each time point was calculated. Nonlinear curve fitting (one phase exponential association) of the fluorescence intensity was performed with GraphPad Prism, where the net recovery after photobleaching is provided by the following equation: $Y=Y0+(Plateau-Y0)\times(1-\exp(-K\times x))$, where Y0 is the Y value when time is zero directly after the bleaching impulse, Plateau is the Y value at infinite times, expressed as a fraction of the fluorescence before bleaching and was used to determine the dynamic actin pool (F-actin dynamic). The stable pool (F-actin stable) is the fraction of fluorescence that does not recover within the imaging period of 95 sec calculated as 1-(F-actin dynamic), K is the rate constant, and τ is the time constant, expressed in s; it is computed as the reciprocal of K.

STED microscopy and image analysis

STED nanoscopy was performed using a Leica SP8-3xSTED and an Abberior Facility line imaging system. The Leica SP8-3xSTED microscope was used for the acquisition of three colour STED images. A white light laser was used for excitation at the wavelengths 488 nm for Alexa-488, 580 nm for Abberior-580 and 650 nm for Atto-647N. Fluorophore depletion was achieved with a 775 nm laser for AttoFluor-647N/ Abberior-580 and a 592 nm laser for Alexa-488. All images were acquired using a 100x oil objective (Leica, HC APO CS2). Emission light was detected in bins: 660-730 nm for Atto-647N, 590-620 nm for Abberior-580 and 500-530 nm for Alexa-488. Gated detection was applied with a delay of 0.3 to 1.5 nanosecond. Pinhole size was set to 1 AU. Images were acquired with a 5x zoom resulting in a pixel size of 22,73 nm, 1024 by 1024 and a 16x line averaging.

Additional STED imaging was performed on an Abberior STED Facility line microscope (Abberior Instruments GmbH) with an UPLSAPO 100x oil immersion objective lens (NA 1.4). Pixel size was set to 20 nm for all images. Images were obtained from a 16x frame accumulation. Excitation was achieved with pulsed diode lasers PDL-T 488, 561

and 640. Both the red and far-red channel were depleted using a 775 nm laser (PFL-40-3000-775-B1R). Pinhole size was set to 1AU. Gated detection was applied for both channels.

Postsynaptic distribution of CAP1 was analyzed in mushroom-like spines of two independent DIV16 hippocampal cultures using a custom-written script in MATLAB (R2015a, MathWorks, Inc) that has been described previously (Mikhaylova, 2018). Postsynaptic distribution of phalloidin, Shank3, PSD-95 and Homer in mushroom-like spines from CTR and CAP1-KO neurons has been analyzed in three independent DIV16 hippocampal cultures. Line scan analysis was carried out with FIJI 'plot profile' tool (line width:15).

Proximity ligation assay

Rat hippocampal neuronal primary cultures were prepared from embryonic day 19 (E19) rat hippocampi as previously described (Piccoli, 2007). Primary hippocampal cultures were transfected with GFP at DIV9-10 and fixed at DIV15 with 4% PFA/sucrose in PBS for 10 min at room temperature (RT), then washed three times with PBS. Neurons were permeabilized with 0.1% Triton X-100 in PBS for 15 min at RT. After incubation with the blocking solution of the PLA kit (Duolink® PLA Technology), cells were incubated o/n at 4°C with primary antibodies against CAP1 (1:100, Abnova, H00010487-M02) and cofilin1 (1:100, Cell Signaling, 5175). According to the manufacturer's instructions, after 2 washes with Wash Buffer A, secondary antibodies conjugated with oligonucleotides were added and the oligonucleotides of the bound probes were ligated and amplified by a fluorescent polymerase that visualizes the PLA clusters. Coverslips were then washed 3 times with decreasing concentration of Buffer Solution B. After this, cells were labelled with primary antibody against GFP (1:500, Millipore, AB16901) for 1 h at RT, washed and then incubated with secondary antibody. After 3 washes with PBS, coverslips were mounted on slides in Fluoromount™ Aqueous Mounting Medium (Sigma-Aldrich).

Protein extraction and synaptosomes

Prefrontal cortices were snap frozen in liquid N_2 and stored at -80°C. Homogenization was done with 6-10 strokes in 750 µl lysis buffer (50 mM Tris-pH 7.5, 150 mM NaCl, 1% Triton-X100, 1x Complete Protease Inhibitor Cocktail, Roche) using a dounce homogenizer. After 20 min centrifugation, 100 µl supernatant was collected and used

for further analysis. Protein lysates from isolated neurons were generated from five coverslips (250,000 neurons/coverslip) by treating with 50 µl lysis buffer incl. PST (1x PhosSTOP, Roche) on ice. After 10 min incubation on the shaker at 4°C, neurons were lysed by pipetting 10 times up and down.

Synaptosomes were purified as described (Lopes, 1999). Briefly, prefrontal brain tissue was homogenized in chilled sucrose solution (0.32 M sucrose, 1 mM EDTA, 1 mg/ml bovine serum albumin, 5 mM HEPES, pH 7.4) with 8 strokes using a dounce homogenizer. After removing nuclei and cell debris by centrifugation (3,000 g, 10 min, 4°C), supernatant was further pelleted at 14,000 g for 10 min at 4°C. A pellet containing synaptosomes was enriched on a floatation gradient containing 45% Percoll in Krebs-Ringer solution (140 mM NaCl, 5 mM KCl, 25 mM HEPES, 1 mM EDTA, 10 mM glucose, pH 7.4), and the supernatant (S2) containing microsomes and soluble enzymes was stored at -80°C. The synaptosomal fraction was resuspended in Krebs-HEPES solution (124 mM NaCl, 3 mM KCl, 1 mM MgCl2, 2 mM $CaCl_2$, and 10 mM glucose buffered with 25 mM HEPES, pH 7.4) for subsequent use. For solubilization, synaptosomes were diluted 1:1 with ice-cold 0.1 mM $CaCl_2$, then an equal volume of 2 x solubilization buffer (2% TX-100, 0.2 mM $CaCl_2$, 40 mM Tris buffer, pH 7.4) was added. Soluble or membrane associated synaptic proteins were separated by centrifugation at 10,000 g for 30 min at 4°C.

Proteins were separated on a 10% SDS-PAGE and transferred o/n at 4°C and 27 V onto a poly-vinylidene difluoride membrane (GE Healthcare) using Mini-Protean electrophoresis system (Biorad). Non-specific antibody binding was blocked in Tris-buffered saline containing 5% milk powder and 0.2% Tween 20 (TBS-T/milk). Membranes were incubated with primary antibody diluted in TBST-T/milk dilutions for 2 hours at RT. Thereafter, membranes were washed three with TBS-T/milk and incubated with horseradish peroxidase-conjugated secondary antibodies (Thermo Fisher Scientific) in TBS-T/milk for 1 h. Membranes were washed three times with TBS-T before developing with Amersham ECLplus reagent (GE Healthcare). Tables S2-3 include lists of antibodies.

Co-immunoprecipitation with hippocampal homogenates

Mouse hippocampi were homogenized at 4 °C in an ice-cold buffer with Roche Complete™ Protease Inhibitor Cocktail, phosphatase inhibitors (PhosSTOP™, Sigma-

Aldrich), 0.32 M Sucrose, 1 mM HEPES, 1 mM NaF, 0.1 mM PMSF, 1 mM MgCl2 using a glass-teflon homogenizer. Aliquots of 50 µg of homogenate obtained from mouse hippocampus were incubated for 1 h at 4 °C in 200 µL of RIPA buffer (200 mM NaCl, 10 mM EDTA, 10 mM Na_2HPO_4, 0.5% NP-40, 0.1% SDS) and SureBeads Protein A magnetic beads (Bio-Rad) as pre-cleaning procedure. The supernatant was incubated with primary antibody against CAP1 (Abnova, H00010487-M02) o/n at 4°C. SureBeads Protein A magnetic beads were added and incubation was continued for 2 h at RT. After 3 washes with RIA buffer, beads were resuspended in sample buffer and heated for 10 min. Beads were collected by centrifugation and all supernatants were applied onto SDS-PAGE. The precipitated immunocomplex was analyzed by anti-cofilin1 (Cell Signaling, #5175) and anti-CAP1 antibody (Proteintech, 16231-1-AP).

Co-immunoprecipitation in HT-22 cells

For each CoIP assay 50 µL Dynabeads™ Protein G (Invitrogen, #10003D) were used and incubated with 2 µg anti-GFP antibody (Invitrogen, 10362) for 1.5 h on a rotating platform. In the meantime, transfected HT-22 cells were lysed, homogenized and supernatant was obtained after centrifugation. After incubation, magnetic beads were washed three times with CoIP wash buffer (20 mM Tris/HCl pH 8.0, 100 mM NaCl). 600 µL of supernatant for each condition were applied and samples were left for incubation for approximately 2 h at 4°C on a rotating platform. Subsequently beads were washed two times with CoIP wash buffer before resuspension in 120 µL of sample buffer. For validation samples and controls were heated for 5 min and applied onto SDS-PAGE. Afterwards, proteins were blotted onto a nitrocellulose membrane before incubation with a c-myc monoclonal antibody (Invitrogen, MA1-980). Expression levels of GFP and GFP-cofilin in the inputs were determined by exploiting an anti-GFP antibody (Invitrogen, 10362). Immunoblots were analyzed by using the Odyssey DLx imager (Li-Cor).

Statistical Analysis

Values are reported as mean ± standard error of the mean (SEM) and (if not otherwise stated) based on three independent biological replicates. For data with single comparison statistical significance was calculated using Student's t-test (two-sample, unpaired), comparison of spine type distribution was tested with $\chi 2$-test. In all

experiments, experimenters were blind to the genotype during image acquisition and analysis.

Declarations

Ethics approval and consent to participate

Treatment of mice was in accordance with the German law for conducting animal experiments and followed the guidelines for the care and use of laboratory animals of the U.S. National Institutes of Health. Killing of mice has been approved by internal animal welfare authorities.

Consent for publication

Not applicable

Data availability

The datasets generated during and/or analysed during the current study are available from the corresponding author on reasonable request.

Competing interests

The authors have no relevant financial or non-financial interests to disclose

Funding

This work was supported by research grants from Fondazione Cariplo (2018-0511) and from Deutsche Forschungsgemeinschaft (DFG) RU 1232/7-1 to MBR as well as DFG Emmy Noether Programme MI1923/1-2, FOR2419 TP2, and Excellence Strategy – EXC-2049–390688087 to MM. Abberior STED System was funded by the DFG – INST 276/760-1.

Authors' contributions

Experiments were designed and results were discussed by AH, CS, SK, BvB, DH, MM, TS, SR, EM and MBR. Data were analyzed by AH, CS, TS, RS and SK. Manuscript was written by MBR, AH, CS, EM and SK.

Acknowledgements

We thank Dr. Walter Witke (Bonn, Germany) for Cfl1$^{flx/flx}$ mice and cofilin1 construct, Dr. Robert Grosse (Freiburg, Germany) for LifeAct-GFP construct, Dr. David Solecki (Memphis, USA) for mCherry-Cre constructs, Dr. Kristin Michaelsen-Preusse (Braunschweig, Germany) for GFP-actin and dsRed construct, Eva Becker and Renate Gondrum for excellent technical support, Felix Schneider for support in data presentation and Dalila Colombaretti for support in image analysis. For technical support and access to the STED imaging systems we thank Drs. Oliver Kobler, Manuel Halte, Caroline Kühne and Marc Erhardt.

References

Ackermann M, Matus A (2003) Activity-induced targeting of profilin and stabilization of dendritic spine morphology. Nat Neurosci 6: 1194-200

Bellenchi GC, Gurniak CB, Perlas E, Middei S, Ammassari-Teule M, Witke W (2007) N-cofilin is associated with neuronal migration disorders and cell cycle control in the cerebral cortex. Genes Dev 21: 2347-57

Ben Zablah Y, Merovitch N, Jia Z (2020) The Role of ADF/Cofilin in Synaptic Physiology and Alzheimer's Disease. Front Cell Dev Biol 8: 594998

Bertling E, Hotulainen P, Mattila PK, Matilainen T, Salminen M, Lappalainen P (2004) Cyclase-associated protein 1 (CAP1) promotes cofilin-induced actin dynamics in mammalian nonmuscle cells. Mol Biol Cell 15: 2324-34

Bertling E, Quintero-Monzon O, Mattila PK, Goode BL, Lappalainen P (2007) Mechanism and biological role of profilin-Srv2/CAP interaction. J Cell Sci 120: 1225-34

Bosch M, Castro J, Saneyoshi T, Matsuno H, Sur M, Hayashi Y (2014) Structural and molecular remodeling of dendritic spine substructures during long-term potentiation. Neuron 82: 444-59

Bosch M, Hayashi Y (2012) Structural plasticity of dendritic spines. Curr Opin Neurobiol 22: 383-388

Bourgeron T (2015) From the genetic architecture to synaptic plasticity in autism spectrum disorder. Nat Rev Neurosci 16: 551-63

Colpan M, Iwanski J, Gregorio CC (2021) CAP2 is a regulator of actin pointed end dynamics and myofibrillogenesis in cardiac muscle. Commun Biol 4: 365

Duffney LJ, Zhong P, Wei J, Matas E, Cheng J, Qin L, Ma K, Dietz DM, Kajiwara Y, Buxbaum JD, Yan Z (2015) Autism-like Deficits in Shank3-Deficient Mice Are Rescued by Targeting Actin Regulators. Cell Rep 11: 1400-13

Feuge J, Scharkowski F, Michaelsen-Preusse K, Korte M (2019) FMRP Modulates Activity-Dependent Spine Plasticity by Binding Cofilin1 mRNA and Regulating Localization and Local Translation. Cereb Cortex 29:5204-5216

Field J, Ye DZ, Shinde M, Liu F, Schillinger KJ, Lu M, Wang T, Skettini M, Xiong Y, Brice AK, Chung DC, Patel VV (2015) CAP2 in cardiac conduction, sudden cardiac death and eye development. Sci Rep 5: 17256

Fukazawa Y, Saitoh Y, Ozawa F, Ohta Y, Mizuno K, Inokuchi K (2003) Hippocampal LTP is accompanied by enhanced F-actin content within the dendritic spine that is essential for late LTP maintenance in vivo. Neuron 38: 447-60

Gomez TM, Letourneau PC (2014) Actin dynamics in growth cone motility and navigation. J Neurochem 129: 221-34

Goodson M, Rust MB, Witke W, Bannerman D, Mott R, Ponting CP, Flint J (2012) Cofilin-1: a modulator of anxiety in mice. PLoS Genet 8: e1002970

Görlich A, Wolf M, Zimmermann AM, Gurniak CB, Al Banchaabouchi M, Sassoe-Pognetto M, Witke W, Friauf E, Rust MB (2011) N-Cofilin Can Compensate for the Loss of ADF in Excitatory Synapses. PLoS One 6: e26789

Gu J, Lee CW, Fan Y, Komlos D, Tang X, Sun C, Yu K, Hartzell HC, Chen G, Bamburg JR, Zheng JQ (2010) ADF/cofilin-mediated actin dynamics regulate AMPA receptor trafficking during synaptic plasticity. Nat Neurosci 13: 1208-15

Gurniak CB, Chevessier F, Jokwitz M, Jonsson F, Perlas E, Richter H, Matern G, Boyl PP, Chaponnier C, Furst D, Schroder R, Witke W (2014) Severe protein aggregate myopathy in a knockout mouse model points to an essential role of cofilin2 in sarcomeric actin exchange and muscle maintenance. Eur J Cell Biol 93: 252-266

Herde MK, Friauf E, Rust MB (2010) Developmental expression of the actin depolymerizing factor ADF in the mouse inner ear and spiral ganglia. J Comp Neurol 518: 1724-1741

Hering H, Sheng M (2001) Dendritic spines: structure, dynamics and regulation. Nat Rev Neurosci 2: 880-8

Hild G, Kalmar L, Kardos R, Nyitrai M, Bugyi B (2014) The other side of the coin: functional and structural versatility of ADF/cofilins. Eur J Cell Biol 93: 238-51

Hlushchenko I, Koskinen M, Hotulainen P (2016) Dendritic spine actin dynamics in neuronal maturation and synaptic plasticity. Cytoskeleton (Hoboken) 73: 435-41

Hotulainen P, Llano O, Smirnov S, Tanhuanpaa K, Faix J, Rivera C, Lappalainen P (2009) Defining mechanisms of actin polymerization and depolymerization during dendritic spine morphogenesis. J Cell Biol 185: 323-39

Jang HD, Lee SE, Yang J, Lee HC, Shin D, Lee H, Lee J, Jin S, Kim S, Lee SJ, You J, Park HW, Nam KY, Lee SH, Park SW, Kim JS, Kim SY, Kwon YW, Kwak SH, Yang HM et al. (2019) Cyclase-associated protein 1 is a binding partner of proprotein convertase subtilisin/kexin type-9 and is required for the degradation of low-density lipoprotein receptors by proprotein convertase subtilisin/kexin type-9. Eur Heart J 41: 239-252

Jansen S, Collins A, Golden L, Sokolova O, Goode BL (2014) Structure and mechanism of mouse cyclase-associated protein (CAP1) in regulating actin dynamics. J Biol Chem 289: 30732-42

Johnston AB, Collins A, Goode BL (2015) High-speed depolymerization at actin filament ends jointly catalysed by Twinfilin and Srv2/CAP. Nat Cell Biol 17: 1504-11

Kakurina GV, Kolegova ES, Kondakova IV (2018) Adenylyl Cyclase-Associated Protein 1: Structure, Regulation, and Participation in Cellular Processes. Biochemistry (Mosc) 83: 45-53

Kepser LJ, Damar F, De Cicco T, Chaponnier C, Proszynski TJ, Pagenstecher A, Rust MB (2019) CAP2 deficiency delays myofibril actin cytoskeleton differentiation and disturbs skeletal muscle architecture and function. Proc Natl Acad Sci USA 116: 8397-8402

Kotila T, Kogan K, Enkavi G, Guo S, Vattulainen I, Goode BL, Lappalainen P (2018) Structural basis of actin monomer re-charging by cyclase-associated protein. Nat Commun 9: 1892

Kotila T, Wioland H, Enkavi G, Kogan K, Vattulainen I, Jegou A, Romet-Lemonne G, Lappalainen P (2019) Mechanism of synergistic actin filament pointed end depolymerization by cyclase-associated protein and cofilin. Nat Commun 10: 5320

Kumar A, Paeger L, Kosmas K, Kloppenburg P, Noegel AA, Peche VS (2016) Neuronal Actin Dynamics, Spine Density and Neuronal Dendritic Complexity Are Regulated by CAP2. Front Cell Neurosci 10: 180

Lamprecht R, Farb CR, Rodrigues SM, LeDoux JE (2006) Fear conditioning drives profilin into amygdala dendritic spines. Nat Neurosci 9: 481-3

Lin YC, Yeckel MF, Koleske AJ (2013) Abl2/Arg controls dendritic spine and dendrite arbor stability via distinct cytoskeletal control pathways. J Neurosci 33: 1846-57

Liu H, Naismith JH (2008) An efficient one-step site-directed deletion, insertion, single and multiple-site plasmid mutagenesis protocol. BMC Biotechnol 8: 91

Lopes LV, Cunha RA, Ribeiro JA (1999) Cross talk between A(1) and A(2A) adenosine receptors in the hippocampus and cortex of young adult and old rats. J Neurophysiol 82: 3196-203

Ma XM, Miller MB, Vishwanatha KS, Gross MJ, Wang Y, Abbott T, Lam TT, Mains RE, Eipper BA (2014) Nonenzymatic domains of Kalirin7 contribute to spine morphogenesis through interactions with phosphoinositides and Abl. Mol Biol Cell 25: 1458-71

Makkonen M, Bertling E, Chebotareva NA, Baum J, Lappalainen P (2013) Mammalian and malaria parasite cyclase-associated proteins catalyze nucleotide exchange on G-actin through a conserved mechanism. J Biol Chem 288: 984-94

Meng Y, Zhang Y, Tregoubov V, Janus C, Cruz L, Jackson M, Lu WY, MacDonald JF, Wang JY, Falls DL, Jia Z (2002) Abnormal spine morphology and enhanced LTP in LIMK-1 knockout mice. Neuron 35: 121-33

Michaelsen-Preusse K, Zessin S, Grigoryan G, Scharkowski F, Feuge J, Remus A, Korte M (2016) Neuronal profilins in health and disease: Relevance for spine plasticity and Fragile X syndrome. Proc Natl Acad Sci USA 113: 3365-70

Michaelsen K, Murk K, Zagrebelsky M, Dreznjak A, Jockusch BM, Rothkegel M, Korte M (2010) Fine-tuning of neuronal architecture requires two profilin isoforms. Proc Natl Acad Sci USA 107: 15780-5

Mikhaylova M, Bar J, van Bommel B, Schatzle P, YuanXiang P, Raman R, Hradsky J, Konietzny A, Loktionov EY, Reddy PP, Lopez-Rojas J, Spilker C, Kobler O, Raza SA, Stork O, Hoogenraad CC, Kreutz MR (2018) Caldendrin Directly Couples Postsynaptic Calcium Signals to Actin Remodeling in Dendritic Spines. Neuron 97: 1110-1125 e14

Moeller ML, Shi Y, Reichardt LF, Ethell IM (2006) EphB receptors regulate dendritic spine morphogenesis through the recruitment/phosphorylation of focal adhesion kinase and RhoA activation. J Biol Chem 281: 1587-98

Ochs SM, Dorostkar MM, Aramuni G, Schon C, Filser S, Poschl J, Kremer A, Van Leuven F, Ovsepian SV, Herms J (2015) Loss of neuronal GSK3beta reduces dendritic spine stability and attenuates excitatory synaptic transmission via beta-catenin. Mol Psychiatry 20: 482-9

Omar MH, Kerrisk Campbell M, Xiao X, Zhong Q, Brunken WJ, Miner JH, Greer CA, Koleske AJ (2017) CNS Neurons Deposit Laminin alpha5 to Stabilize Synapses. Cell Rep 21: 1281-1292

Omotade OF, Pollitt SL, Zheng JQ (2017) Actin-based growth cone motility and guidance. Mol Cell Neurosci 84: 4-10

Ono S (2013) The role of cyclase-associated protein in regulating actin filament dynamics - more than a monomer-sequestration factor. J Cell Sci 126: 3249-58

Peche VS, Holak TA, Burgute BD, Kosmas K, Kale SP, Wunderlich FT, Elhamine F, Stehle R, Pfitzer G, Nohroudi K, Addicks K, Stockigt F, Schrickel JW, Gallinger J, Schleicher M, Noegel AA (2012) Ablation of cyclase-associated protein 2 (CAP2) leads to cardiomyopathy. Cell Mol Life Sci 70:527-543

Peineau S, Taghibiglou C, Bradley C, Wong TP, Liu L, Lu J, Lo E, Wu D, Saule E, Bouschet T, Matthews P, Isaac JT, Bortolotto ZA, Wang YT, Collingridge GL (2007) LTP inhibits LTD in the hippocampus via regulation of GSK3beta. Neuron 53: 703-17

Pelucchi S, Vandermeulen L, Pizzamiglio L, Aksan B, Yan J, Konietzny A, Bonomi E, Borroni B, Padovani A, Rust MB, Di Marino D, Mikhaylova M, Mauceri D, Antonucci F, Edefonti V, Gardoni F, Di Luca M, Marcello E (2020) Cyclase-associated protein 2 dimerization regulates cofilin in synaptic plasticity and Alzheimer's disease. Brain Commun 2: fcaa086

Piccoli G, Verpelli C, Tonna N, Romorini S, Alessio M, Nairn AC, Bachi A, Sala C (2007) Proteomic analysis of activity-dependent synaptic plasticity in hippocampal neurons. J Proteome Res 6: 3203–3215.

Pontrello CG, Sun MY, Lin A, Fiacco TA, DeFea KA, Ethell IM (2012) Cofilin under control of beta-arrestin-2 in NMDA-dependent dendritic spine plasticity, long-term depression (LTD), and learning. Proc Natl Acad Sci USA 109: E442-51

Pyronneau A, He Q, Hwang JY, Porch M, Contractor A, Zukin RS (2017) Aberrant Rac1-cofilin signaling mediates defects in dendritic spines, synaptic function, and sensory perception in fragile X syndrome. Sci Signal 10: eaan0852

Racz B, Weinberg RJ (2006) Spatial organization of cofilin in dendritic spines. Neuroscience 138: 447-56

Rishal I, Golani O, Rajman M, Costa B, Ben-Yaakov K, Schoenmann Z, Yaron A, Basri R, Fainzilber M, Galun M (2013) WIS-NeuroMath enables versatile high throughput analyses of neuronal processes. Dev Neurobiol 73: 247-56

Rust MB (2015a) ADF/cofilin: a crucial regulator of synapse physiology and behavior. Cell Mol Life Sci 72: 3521-3529

Rust MB (2015b) Novel functions for ADF/cofilin in excitatory synapses - lessons from gene-targeted mice. Commun Integr Biol 8: e1114194

Rust MB, Gurniak CB, Renner M, Vara H, Morando L, Gorlich A, Sassoe-Pognetto M, Banchaabouchi MA, Giustetto M, Triller A, Choquet D, Witke W (2010) Learning, AMPA receptor mobility and synaptic plasticity depend on n-cofilin-mediated actin dynamics. EMBO J 29: 1889-902

Rust MB, Khudayberdiev S, Pelucchi S, Marcello E (2020) CAPt'n of Actin Dynamics: Recent Advances in the Molecular, Developmental and Physiological Functions of Cyclase-Associated Protein (CAP). Front Cell Dev Biol 8: 586631

Rust MB, Maritzen T (2015c) Relevance of presynaptic actin dynamics for synapse function and mouse behavior. Exp Cell Res 335: 165-171

Schneider F, Duong TA, Metz I, Winkelmeier J, Hubner CA, Endesfelder U, Rust MB (2021a) Mutual functional dependence of cyclase-associated protein 1 (CAP1) and cofilin1 in neuronal actin dynamics and growth cone function. Prog Neurobiol 202: 102050

Schneider F, Duong TA, Rust MB (2021b) Neuron Replating, a Powerful and Versatile Approach to Study Early Aspects of Neuron Differentiation. eNeuro 8: ENEURO.0536-20.2021

Schneider F, Metz I, Khudayberdiev S, Rust MB (2021c) Functional Redundancy of Cyclase-Associated Proteins CAP1 and CAP2 in Differentiating Neurons. Cells 10

Schratt GM, Tuebing F, Nigh EA, Kane CG, Sabatini ME, Kiebler M, Greenberg ME (2006) A brain-specific microRNA regulates dendritic spine development. Nature 439: 283-9

Shekhar S, Chung J, Kondev J, Gelles J, Goode BL (2019) Synergy between Cyclase-associated protein and Cofilin accelerates actin filament depolymerization by two orders of magnitude. Nat Commun 10: 5319

Sheng M, Hoogenraad CC (2007) The postsynaptic architecture of excitatory synapses: a more quantitative view. Annu Rev Biochem 76: 823-47

Shi Y, Pontrello CG, DeFea KA, Reichardt LF, Ethell IM (2009) Focal adhesion kinase acts downstream of EphB receptors to maintain mature dendritic spines by regulating cofilin activity. J Neurosci 29: 8129-42

Spence EF, Soderling SH (2015) Actin Out: Regulation of the Synaptic Cytoskeleton. J Biol Chem 290: 28613-22

Sungur AO, Stemmler L, Wohr M, Rust MB (2018) Impaired Object Recognition but Normal Social Behavior and Ultrasonic Communication in Cofilin1 Mutant Mice. Front Behav Neurosci 12: 25

Tian L, Stefanidakis M, Ning L, Van Lint P, Nyman-Huttunen H, Libert C, Itohara S, Mishina M, Rauvala H, Gahmberg CG (2007) Activation of NMDA receptors promotes dendritic spine development through MMP-mediated ICAM-5 cleavage. J Cell Biol 178: 687-700

Tronche F, Kellendonk C, Kretz O, Gass P, Anlag K, Orban PC, Bock R, Klein R, Schutz G (1999) Disruption of the glucocorticoid receptor gene in the nervous system results in reduced anxiety. Nat Genet 23: 99-103

Wang XB, Bozdagi O, Nikitczuk JS, Zhai ZW, Zhou Q, Huntley GW (2008) Extracellular proteolysis by matrix metalloproteinase-9 drives dendritic spine enlargement and long-term potentiation coordinately. Proc Natl Acad Sci USA 105: 19520-5

Wolf M, Zimmermann AM, Gorlich A, Gurniak CB, Sassoe-Pognetto M, Friauf E, Witke W, Rust MB (2015) ADF/Cofilin Controls Synaptic Actin Dynamics and Regulates Synaptic Vesicle Mobilization and Exocytosis. Cereb Cortex 25: 2863-75

Zhou Q, Homma KJ, Poo MM (2004) Shrinkage of dendritic spines associated with long-term depression of hippocampal synapses. Neuron 44: 749-57

Zimmermann AM, Jene T, Wolf M, Gorlich A, Gurniak CB, Sassoe-Pognetto M, Witke W, Friauf E, Rust MB (2015) Attention-Deficit/Hyperactivity Disorder-like Phenotype in a Mouse Model with Impaired Actin Dynamics. Biol Psychiatry 78: 95-106

Legends to main figure

Figure 1. Enrichment of CAP1 in spine heads. (A) Immunoblots showing CAP1 expression in cerebral cortex lysates throughout postnatal development. GAPDH was used as loading control. **(B)** Immunoblots showing CAP1 expression in isolated cerebral cortex neurons. β-tubulin was used as loading control. **(C)** Immunoblots showing presence of CAP1 in synaptosomes and in the soluble, but not in the insoluble synaptosomal protein fraction. PSD-95 and synaptophysin proved separation of protein fractions. **(D)** DIV16 hippocampal neurons expressing the volume marker dsRed (red) together with either GFP or CAP1-GFP (green). Boxes indicate areas shown with higher magnification. **(E)** Fluorescence intensity profiles for GFP and dsRed along white lines (labelled E1, E2) shown in left magnified micrograph in D. **(F)** Fluorescence intensity profiles for CAP1-GFP and dsRed along white lines (labelled F1, F2) shown in right magnified micrograph in D. **(G)** Graph showing ratio of GFP and CAP1-GFP intensity in spine heads vs dendritic shaft and in spine heads vs spine neck. **(H)** STED image of a neuron stained with antibodies against CAP1 (green), the PSD marker Shank3 (red) and the presynaptic marker Bassoon (blue). **(I)** Fluorescence intensity profiles for all three proteins along the box in H. **(J)** STED image of a neuron stained with antibodies against CAP1 (green) and Shank3 (red) as well as the F-actin marker phalloidin (blue). **(K)** Graphs showing distribution of CAP1, Shank3 and phalloidin in spine heads. Scheme on the left shows the mask that was used for this analysis. **(L)** Graph showing center of mass for CAP1, Shank3 and phalloidin. Coordinate system's origin indicates center of the spine (see scheme in K). Scale bars (µm): 1 (H, J), 2 (D, high magnification), 20 (D, overview). *: $P<0.05$, ***: $P<0.001$.

Figure 2. Reduced spine density and increased spine size in CAP1-KO neurons. **(A)** Micrographs of CTR and CAP1-KO neurons expressing GFP (green). Boxes indicate areas shown at higher magnification. Graphs showing **(B)** total spine density, **(C)** spine volume, **(D)** total spine length, **(E)** spine head length and **(F)** spine head widths in CTR and CAP1-KO neurons. **(G)** Graph showing fractions of spine types in CTR and CAP1-KO neurons. Scale bar (µm): 2 (A, high magnification) 20 (A, overview). ns: $P\geq0.05$, **: $P<0.01$, ***: $P<0.001$.

Figure 3. CAP1 controls F-actin organization and actin dynamics in spines. (A) Graph showing morphometric analysis of mushroom-like spines in CAP1-KO neurons. **(B)** Image sequence of mushroom-like spines from CTR and CAP1-KO neurons expressing GFP-actin during fluorescent recovery after photobleaching (FRAP). **(C)** Graphs showing GFP-actin recovery curve, **(D)** stable actin fraction and **(E)** half-recovery time of GFP-actin in spines. **(F)** STED images showing mushroom-like spines of GFP-expressing CTR and CAP1-KO neurons (green). Neurons were stained with either phalloidin (blue) and an antibody against Shank3 (red) or with antibodies against Homer (magenta) and PSD-95 (cyan). **(G)** Distribution of fluorescence intensities of phalloidin, Shank3, PSD-95 and Homer in CTR and CAP1-KO spines. GFP was used to determine spine morphology. Relative fluorescence intensities were plotted for each sector as shown in Fig. 1K. **(H)** Graph showing centers of mass for phalloidin, Shank3, PSD-95 and Homer and in CTR and CAP1-KO spines. Centers of mass were normalized to GFP. Scale bars (µm): 1 (B, F). ns: $P \geq 0.05$, *: $P < 0.05$, **: $P < 0.01$.

Figure 4. Helical folded domain and CARP domain are relevant for CAP1 function in spines. **(A)** Scheme showing domain structure of myc-tagged CAP1 as well as the mutations introduced into CAP1-HFD, CAP1-CARP and CAP1-P1 constructs. Amino acid residues shown in red were replaced by alanine. OD: oligomerization domain, HFD: helical folded domain, P1: proline-rich domain 1, WH2: Wiskott-Aldrich syndrome homology domain 2, P2: proline-rich domain 2, CARP: CAP and retinitis pigmentosa protein 2 domain. **(B)** Micrographs showing myc antibody staining and GFP in CTR and CAP1-KO neurons expressing myc-tagged WT-CAP1 or myc-tagged CAP1 mutant constructs. Graphs showing **(C)** spine density and **(D)** spine volume in CTR and CAP1-KO neurons upon expression of WT-CAP1 or CAP1 mutants. Black asterisks and ns above CTR or CAP1-KO values in C and D indicate significance of changes when compared to CTR (furthest left values), blue asterisks and ns above CAP1-KO values indicate significance of changes when compared to CAP1-KO neurons (second values from left). Scale bar (µm): 2. ns: $P \geq 0.05$, *: $P < 0.05$, **: $P < 0.01$, ***: $P < 0.001$.

Figure 5. Physical interaction of CAP1 and cofilin1. (A) Dendritic shaft of a hippocampal neuron expressing cofilin1-GFP (green) and CAP1-mCherry (red). **(B)** Fluorescence intensity profiles for cofilin1-GFP and CAP1-mCherry along white lines shown in A. **(C)** Micrographs of DIV15 hippocampal neuron used for proximity ligation assay (PLA). Neurons were transfected with GFP (green), that served as a volume marker to outline dendritic compartment (line in black-white images on the right). Co-localization of CAP1 and cofilin1 by PLA was performed by exploiting antibodies against endogenous proteins. PLA signal (white signal in left images and black signal in right images, respectively) was only detectable in neurons stained with antibodies against both CAP1 and cofilin1, but not in control neurons stained with an antibody against either CAP1 or cofilin1. **(D)** Immunoblot analysis of proteins precipitated with a mouse monoclonal CAP1 antibody from hippocampal (HIP) homogenate. Cofilin1 coprecipitates with CAP1 in hippocampal homogenate. (+) IP: CAP1 antibody, (-) no IgG. **(E)** Immunoblot with an antibody against myc in lysates from HT-22 cells expressing either myc-WT-CAP1 together with GFP, myc-WT-CAP1 together with GFP-WT-cofilin1 or myc-CAP1-HFD together with GFP-WT-cofilin1. In presence of GFP-WT-cofilin1, an antibody against GFP precipitated myc-WT-CAP1, but not myc-CAP1-HFD. **(F)** Immunoblot with an antibody against GFP antibody demonstrating equal expression of GFP and GFP-WT-cofilin1 in HT-22 cells. Scale bars (µm): 2 (A), 5 (C).

Figure 6. Changes in spine morphology of cofilin1-KO neurons. (A) Micrographs of GFP-expressing CTR and cofilin1-KO neurons. Boxes indicate areas shown at higher magnification. Graphs showing **(B)** spine density and **(C)** spine volume in CTR and cofilin1-KO neurons. Graphs showing **(D)** total spine length, **(E)** spine head length and **(F)** spine head widths in CTR and cofilin1-KO neurons. **(G)** Graph showing relative fraction of spine types in CTR and cofilin1-KO neurons. Scale bar (µm): 2 (A, high magnification), 20 (A, overview). ns: $P \geq 0.05$, *: $P < 0.05$, **: $P < 0.01$, ***: $P < 0.001$.

Figure 7: CAP1 and cofilin1 cannot compensate each other's inactivation in spines (A) Micrographs showing dsRed (red) in GFP-transfected CTR and CAP1-KO neurons as well as dsRed (red) and cofilin1-GFP (green) in cofilin1-GFP-transfected

CTR and CAP1-KO neurons. Graphs showing **(B)** spine density and **(C)** spine volume in CTR and CAP1-KO neurons either expressing GFP or cofilin1-GFP. **(D)** Micrographs showing dsRed (red) in GFP-transfected CTR and cofilin1-KO neurons as well as dsRed (red) and CAP1-GFP (green) in CAP1-GFP-transfected CTR and cofilin1-KO neurons. Graphs showing **(E)** spine density and **(F)** spine volume in CTR and cofilin1-KO neurons either expressing GFP or CAP1-GFP. Scale bars (µm): 2 (A, D). ns: $P \geq 0.05$, **: $P < 0.01$, ***: $P < 0.001$.

Figure 8. Functional interdependence of CAP1 and cofilin1 in spines. (A) Micrographs of GFP-expressing CTR and double-KO (dKO) neurons. Boxes indicate areas shown with higher magnification. Graphs showing **(B)** spine density, **(C)** spine volume, **(D)** total spine length, **(E)** spine head length and **(F)** spine head width in CTR and dKO neurons. **(G)** Graph showing relative fraction of spine types in CTR and dKO neurons. **(H)** Micrographs showing dsRed in CTR neurons as well as in dKO neurons upon transfection of CAP1 and/or cofilin1 constructs as indicated. **(I)** Graph showing spine volume in CTR and dKO neurons upon expression of WT-cofilin1 and/or CAP1 constructs as indicated. Black asterisks and ns above dKO values indicate significance of changes when compared to CTR (furthest left values), purple asterisks and ns above dKO values indicate significance of changes when compared to double mutant neurons (second values from left). Scale bars (µm): 2 (A, high magnification, H), 20 (A, overview). ns: $P \geq 0.05$, *: $P < 0.05$, ***: $P < 0.001$.

Legends to supplementary figures, movies, tables

Figure S1. (A) Dendritic shaft of a hippocampal neuron expressing CAP1-GFP (green) and the F-actin marker mCherry-LifeAct (red). **(B)** Fluorescence intensity profiles along white lines shown in A. **(C)** Antibody staining against endogenous CAP1 (green) in a DIV13 hippocampal neuron expressing dsRed (red). **(D)** Antibody staining against CAP1 (green) and doublecortin (Dcx, red) in DIV13 hippocampal neurons from $CAP1^{flx/flx}$ mice (CTR) and brain-specific CAP1-KO mice. Neurons were additionally stained with the DNA dye Hoechst (blue). White boxes indicate areas shown at higher magnification. Scale bars (µm): 2 (A, C), 20 (D).

Figure S2. Antibody staining against CAP1 (blue) in GFP-transfected DIV16 hippocampal neurons from $CAP1^{flx/flx}$ mice expressing either catalytically active mCherry-Cre (Cre, red) or catalytically inactive mCherry-Cre (Cre-mut, red). Scale bar (µm): 20.

Figure S3. Graphs showing **(A)** number of primary neurites, **(B)** number of branching points, and **(C)** branching point normalized to dendritic length in CTR and CAP1-KO neurons. **(D)** Scheme showing categorization of spine types. Graphs showing **(E)** length and width of filopodia-like spines, **(F)** total length, head length and head width of thin spines as well as **(G)** head length and head width of stubby spines in CTR and CAP1-KO neurons. ns: $P \geq 0.05$.

Figure S4. Graphs showing **(A)** length and width of filopodia-like spines, **(B)** total length, head length and head width of thin spines, **(C)** head length and head width of stubby spines as well as **(D)** total length, head length and head width of mushroom-like spines in CTR and cofilin1-KO neurons. ns: $P \geq 0.05$.

Figure S5. Graphs showing **(A)** length and width of filopodia-like spines, **(B)** total length, head length and head width of thin spines, **(C)** head length and head width of stubby spines as well as **(D)** total length, head length and head width of mushroom-like spines in CTR and dKO neurons. ns: $P \geq 0.05$, *: $P < 0.05$.

Movie S1: Movie showing FRAP of GFP-actin in a mushroom-like spine from a CTR neuron.

Movie S2: Movie showing FRAP of GFP-actin in a mushroom-like spine from a CAP1-KO neuron.

Table S1: List of oligonucleotides used for site-directed mutagenesis on CAP1 constructs

Table S2: List of primary antibodies used for immunocytochemistry (ICC) and immunoblots (IB)

Table S3: List of secondary antibodies used for immunocytochemistry (ICC) and immunoblots (IB)

Figures

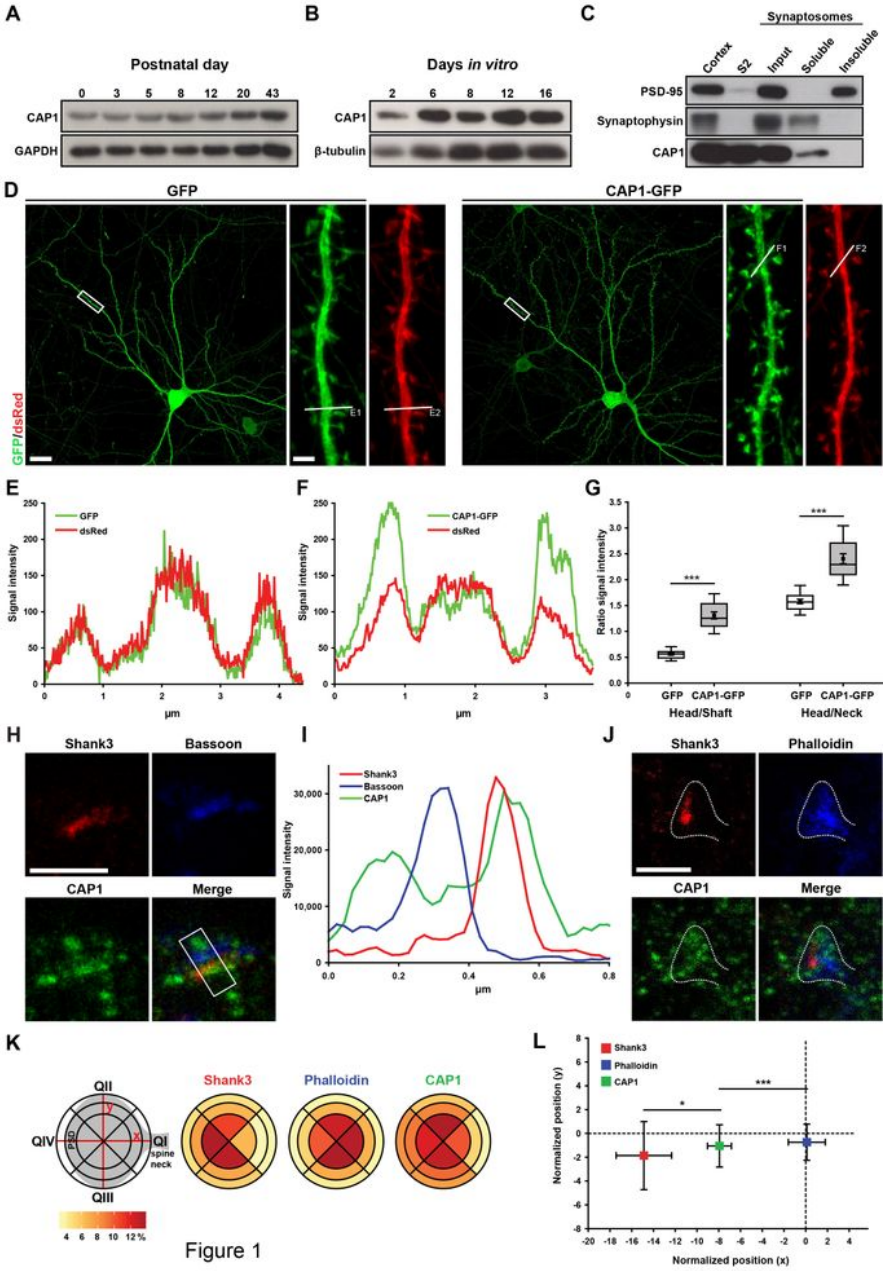

Figure 1

Figure 1

Enrichment of CAP1 in spine heads. (A) Immunoblots showing CAP1 expression in cerebral cortex lysates throughout postnatal development. GAPDH was used as loading control. (B) Immunoblots showing CAP1 expression in isolated cerebral cortex neurons. β-tubulin was used as loading control. (C)

Immunoblots showing presence of CAP1 in synaptosomes and in the soluble, but not in the insoluble synaptosomal protein fraction. PSD-95 and synaptophysin proved separation of protein fractions. (D) DIV16 hippocampal neurons expressing the volume marker dsRed (red) together with either GFP or CAP1-GFP (green). Boxes indicate areas shown with higher magnification. (E) Fluorescence intensity profiles for GFP and dsRed along white lines (labelled E1, E2) shown in left magnified micrograph in D. (F) Fluorescence intensity profiles for CAP1-GFP and dsRed along white lines (labelled F1, F2) shown in right magnified micrograph in D. (G) Graph showing ratio of GFP and CAP1-GFP intensity in spine heads vs dendritic shaft and in spine heads vs spine neck. (H) STED image of a neuron stained with antibodies against CAP1 (green), the PSD marker Shank3 (red) and the presynaptic marker Bassoon (blue). (I) Fluorescence intensity profiles for all three proteins along the box in H. (J) STED image of a neuron stained with antibodies against CAP1 (green) and Shank3 (red) as well as the F-actin marker phalloidin (blue). (K) Graphs showing distribution of CAP1, Shank3 and phalloidin in spine heads. Scheme on the left shows the mask that was used for this analysis. (L) Graph showing center of mass for CAP1, Shank3 and phalloidin. Coordinate system's origin indicates center of the spine (see scheme in K). Scale bars (µm): 1 (H, J), 2 (D, high magnification), 20 (D, overview). *: $P<0.05$, ***: $P<0.001$.

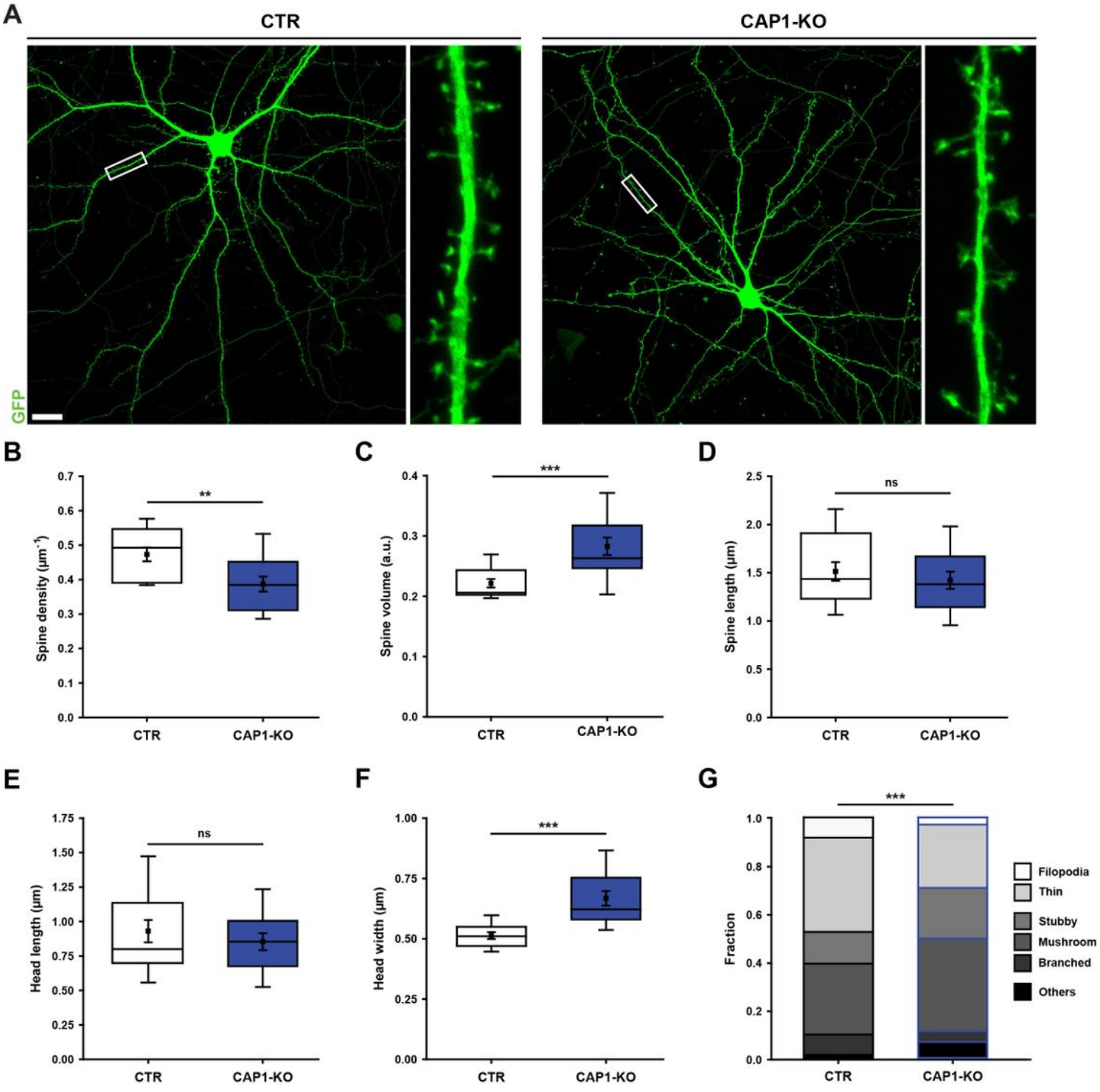

Figure 2

Figure 2

Reduced spine density and increased spine size in CAP1-KO neurons. (A) Micrographs of CTR and CAP1-KO neurons expressing GFP (green). Boxes indicate areas shown at higher magnification. Graphs showing (B) total spine density, (C) spine volume, (D) total spine length, (E) spine head length and (F) spine head widths in CTR and CAP1-KO neurons. (G) Graph showing fractions of spine types in CTR and

CAP1-KO neurons. Scale bar (μm): 2 (A, high magnification) 20 (A, overview). ns: P≥0.05, **: P<0.01, ***: P<0.001.

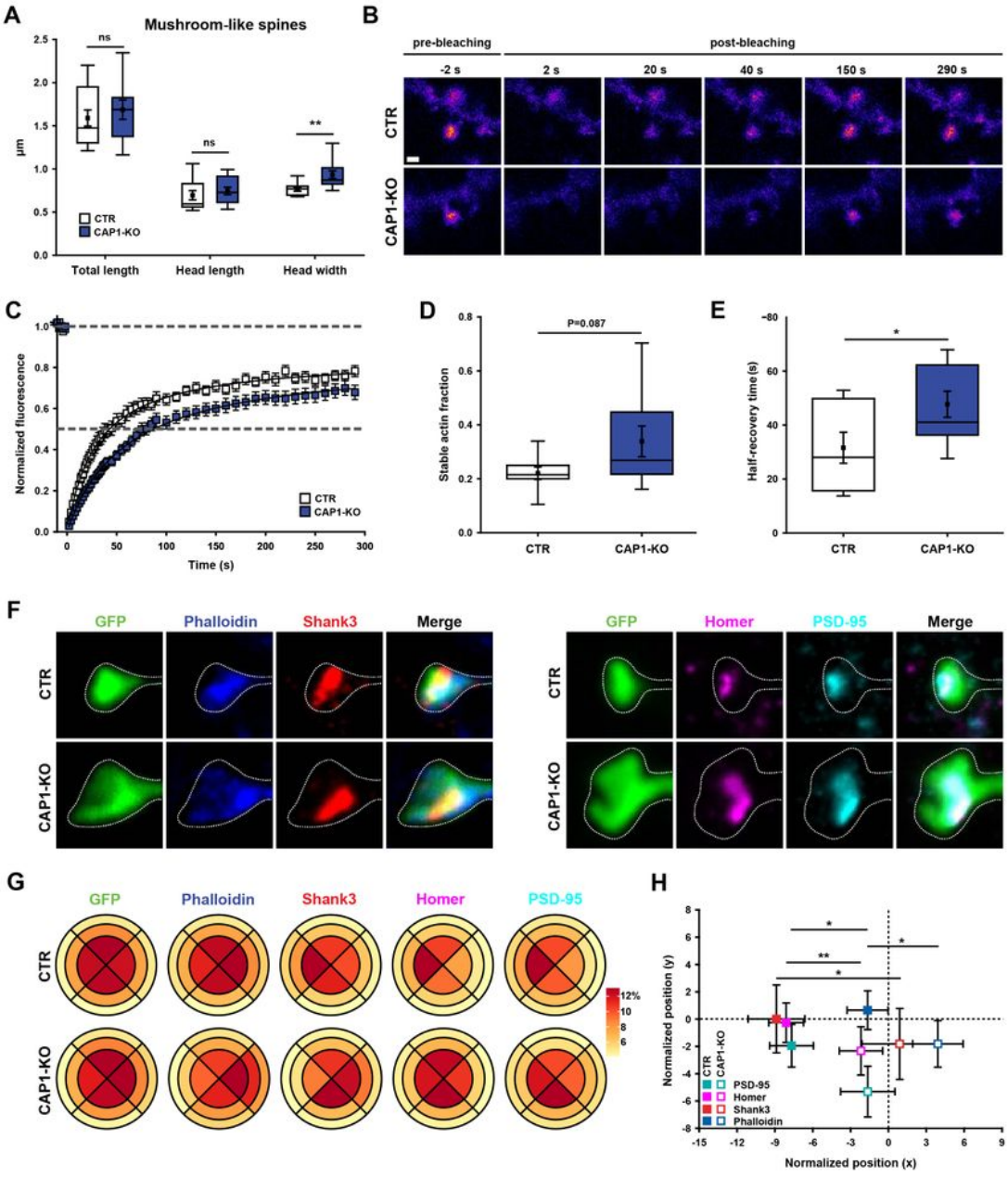

Figure 3

Figure 3

CAP1 controls F-actin organization and actin dynamics in spines. (A) Graph showing morphometric analysis of mushroom-like spines in CAP1-KO neurons. (B) Image sequence of mushroom-like spines

from CTR and CAP1-KO neurons expressing GFP-actin during fluorescent recovery after photobleaching (FRAP). (C) Graphs showing GFP-actin recovery curve, (D) stable actin fraction and (E) half6 recovery time of GFP-actin in spines. (F) STED images showing mushroom-like spines of GFP-expressing CTR and CAP1-KO neurons (green). Neurons were stained with either phalloidin (blue) and an antibody against Shank3 (red) or with antibodies against Homer (magenta) and PSD-95 (cyan). (G) Distribution of fluorescence intensities of phalloidin, Shank3, PSD-95 and Homer in CTR and CAP1-KO spines. GFP was used to determine spine morphology. Relative fluorescence intensities were plotted for each sector as shown in Fig. 1K. (H) Graph showing centers of mass for phalloidin, Shank3, PSD-95 and Homer and in CTR and CAP1-KO spines. Centers of mass were normalized to GFP. Scale bars (μm): 1 (B, F). ns: $P \geq 0.05$, *: $P < 0.05$, **: $P < 0.01$.

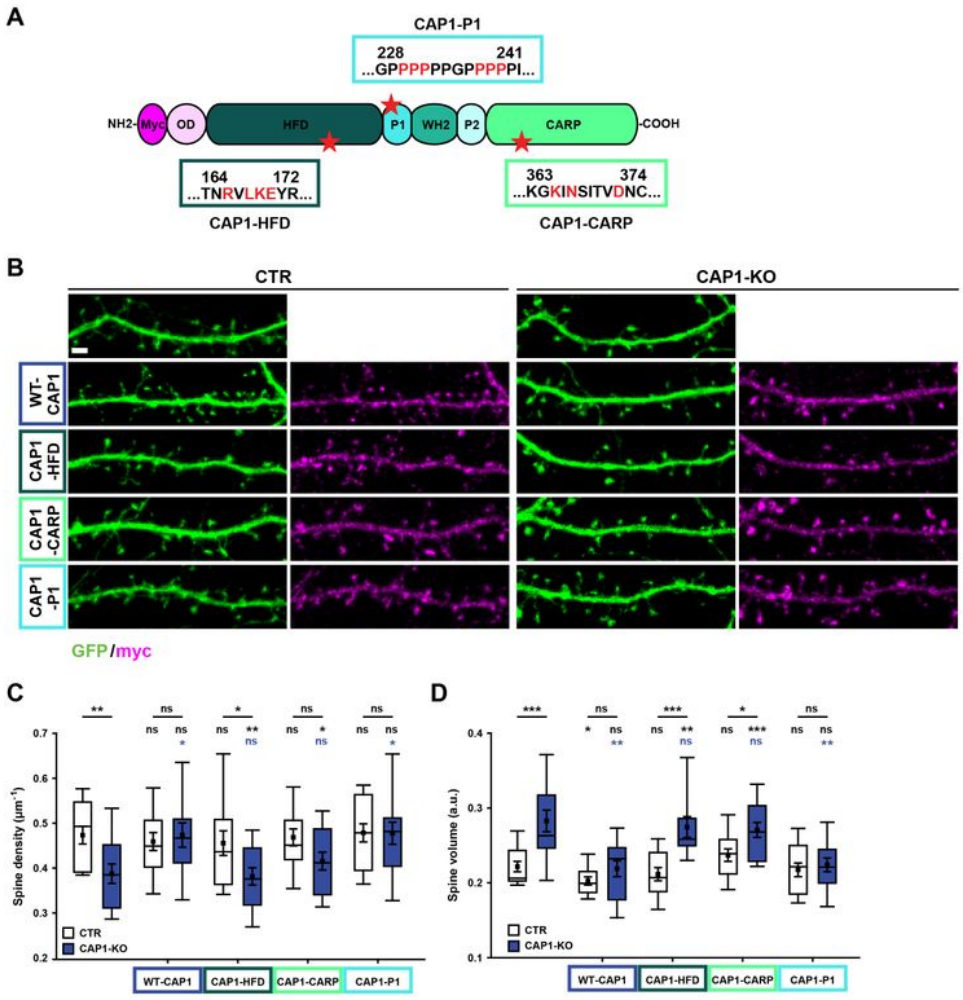

Figure 4

Figure 4

Helical folded domain and CARP domain are relevant for CAP1 function in spines. (A) Scheme showing domain structure of myc-tagged CAP1 as well as the mutations introduced into CAP1-HFD, CAP1-CARP and CAP1-P1 constructs. Amino acid residues shown in red were replaced by alanine. OD: oligomerization domain, HFD: helical folded domain, P1: proline-rich domain 1, WH2: Wiskott-Aldrich syndrome homology domain 2, P2: proline-rich domain 2, CARP: CAP and retinitis pigmentosa protein 2 domain. (B)

Micrographs showing myc antibody staining and GFP in CTR and CAP1-KO neurons expressing myc-tagged WT-CAP1 or myc-tagged CAP1 mutant constructs. Graphs showing (C) spine density and (D) spine volume in CTR and CAP1-KO neurons upon expression of WT-CAP1 or CAP1 mutants. Black asterisks and ns above CTR or CAP1-KO values in C and D indicate significance of changes when compared to CTR (furthest left values), blue asterisks and ns above CAP1-KO values indicate significance of changes when compared to CAP1-KO neurons (second values from left). Scale bar (µm): 2. ns: P≥0.05, *: P<0.05, **: P<0.01, ***: P<0.001.

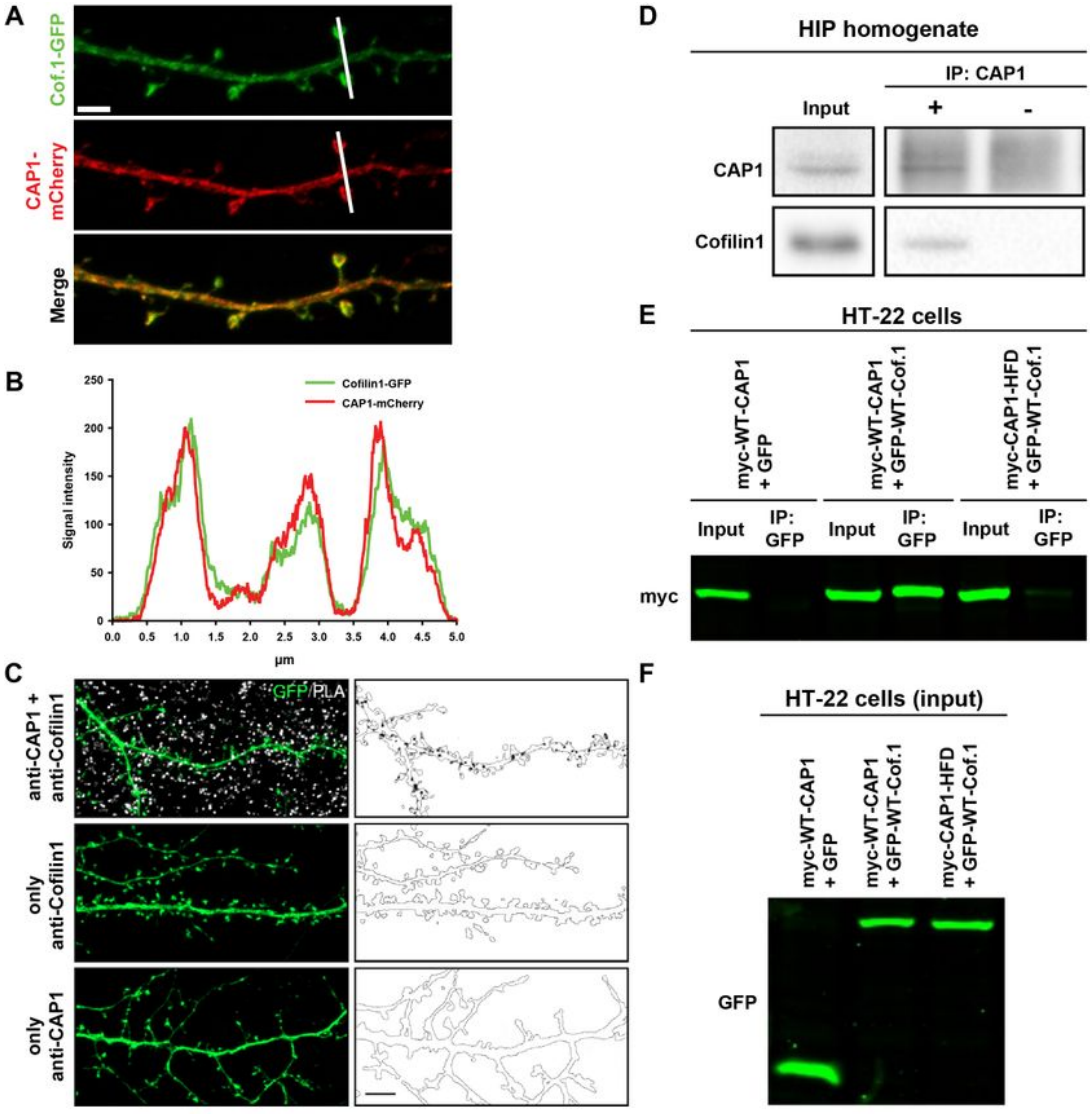

Figure 5

Figure 5

Physical interaction of CAP1 and cofilin1. (A) Dendritic shaft of a hippocampal neuron expressing cofilin1-GFP (green) and CAP1-mCherry (red). (B) Fluorescence intensity profiles for cofilin1-GFP and CAP1-mCherry along white lines shown in A. (C) Micrographs of DIV15 hippocampal neuron used for proximity ligation assay (PLA). Neurons were transfected with GFP (green), that served as a volume marker to outline dendritic compartment (line in black-white images on the right). Co localization of CAP1 and cofilin1 by PLA was performed by exploiting antibodies against endogenous proteins. PLA signal (white signal in left images and black signal in right images, respectively) was only detectable in neurons stained with antibodies against both CAP1 and cofilin1, but not in control neurons stained with an antibody against either CAP1 or cofilin1. (D) Immunoblot analysis of proteins precipitated with a mouse monoclonal CAP1 antibody from hippocampal (HIP) homogenate. Cofilin1 coprecipitates with CAP1 in hippocampal homogenate. (+) IP: CAP1 antibody, (-) no IgG. (E) Immunoblot with an antibody against myc in lysates from HT-22 cells expressing either myc-WT-CAP1 together with GFP, myc-WT-CAP1 together with GFP-WT-cofilin1 or myc-CAP1-HFD together with GFP-WT-cofilin1. In presence of GFP-WT-cofilin1, an antibody against GFP precipitated myc-WT-CAP1, but not myc CAP1-HFD. (F) Immunoblot with an antibody against GFP antibody demonstrating equal expression of GFP and GFP-WT-cofilin1 in HT-22 cells. Scale bars (μm): 2 (A), 20 5 (C).

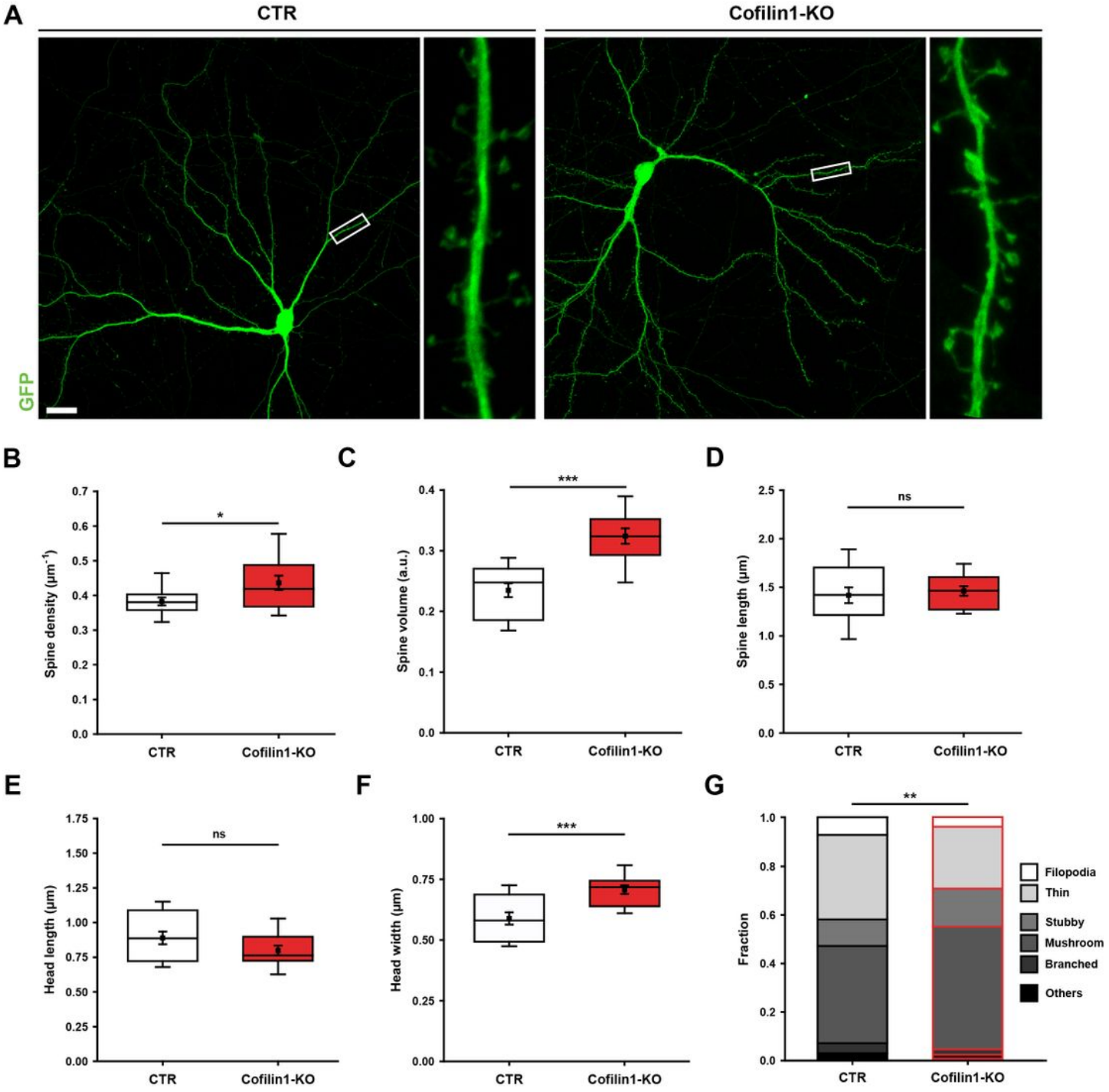

Figure 6

Figure 6

Changes in spine morphology of cofilin1-KO neurons. (A) Micrographs of GFP-expressing CTR and cofilin1-KO neurons. Boxes indicate areas shown at higher magnification. Graphs showing (B) spine density and (C) spine volume in CTR and cofilin1-KO neurons. Graphs showing (D) total spine length, (E) spine head length and (F) spine head widths in CTR and cofilin1-KO neurons. (G) Graph showing relative

fraction of spine types in CTR and cofilin1-KO neurons. Scale bar (μm): 2 (A, high magnification), 20 (A, overview). ns: P≥0.05, *: P<0.05, **: P<0.01, ***: P<0.001.

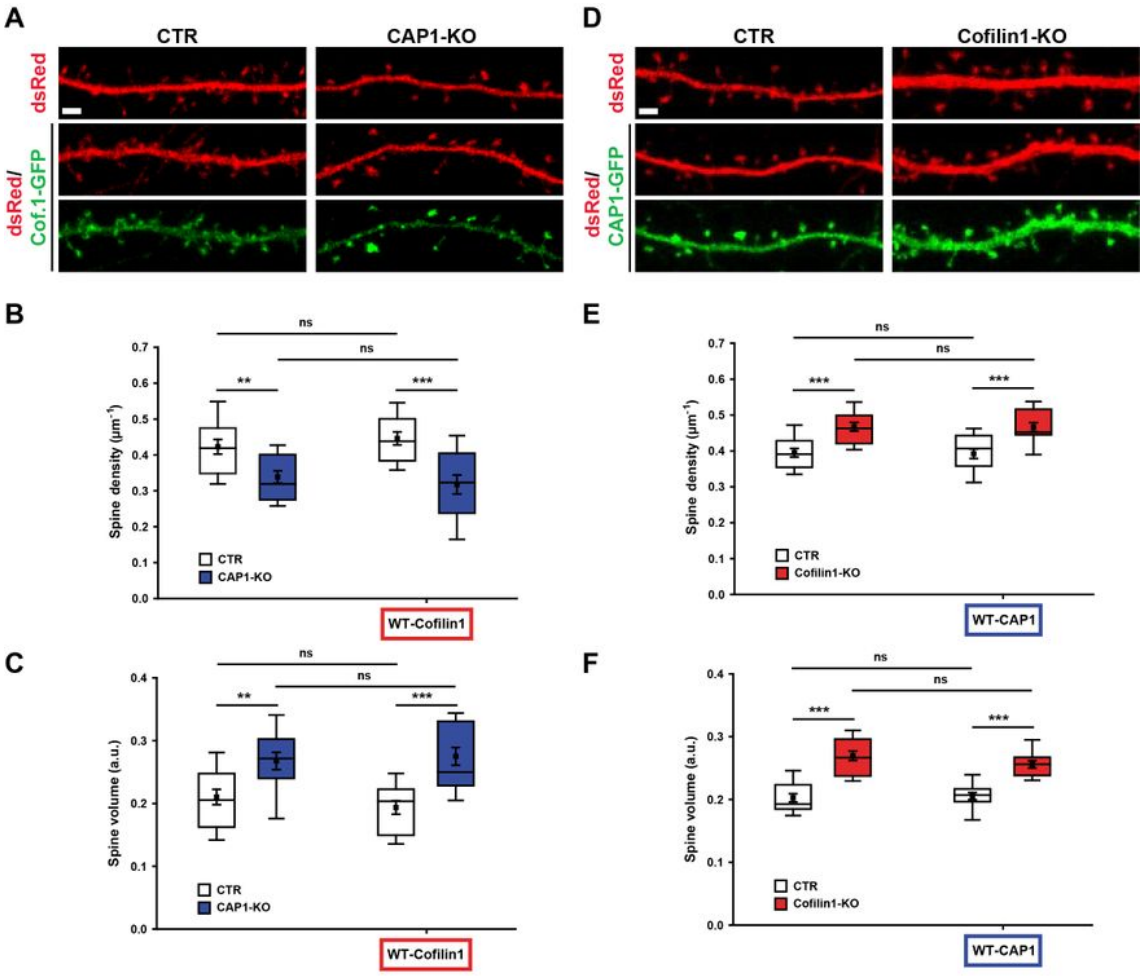

Figure 7

Figure 7

CAP1 and cofilin1 cannot compensate each other's inactivation in spines (A) Micrographs showing dsRed (red) in GFP-transfected CTR and CAP1-KO neurons as well as dsRed (red) and cofilin1-GFP

(green) in cofilin1-GFP-transfected CTR and CAP1-KO neurons. Graphs showing (B) spine density and (C) spine volume in CTR and CAP1-KO neurons either expressing GFP or cofilin1-GFP. (D) Micrographs showing dsRed (red) in GFP-transfected CTR and cofilin1-KO neurons as well as dsRed (red) and CAP1-GFP (green) in CAP1-GFP-transfected CTR and cofilin1-KO neurons. Graphs showing (E) spine density and (F) spine volume in CTR and cofilin1- KO neurons either expressing GFP or CAP1-GFP. Scale bars (µm): 2 (A, D). ns: P≥0.05, **: P<0.01, ***: P<0.001.

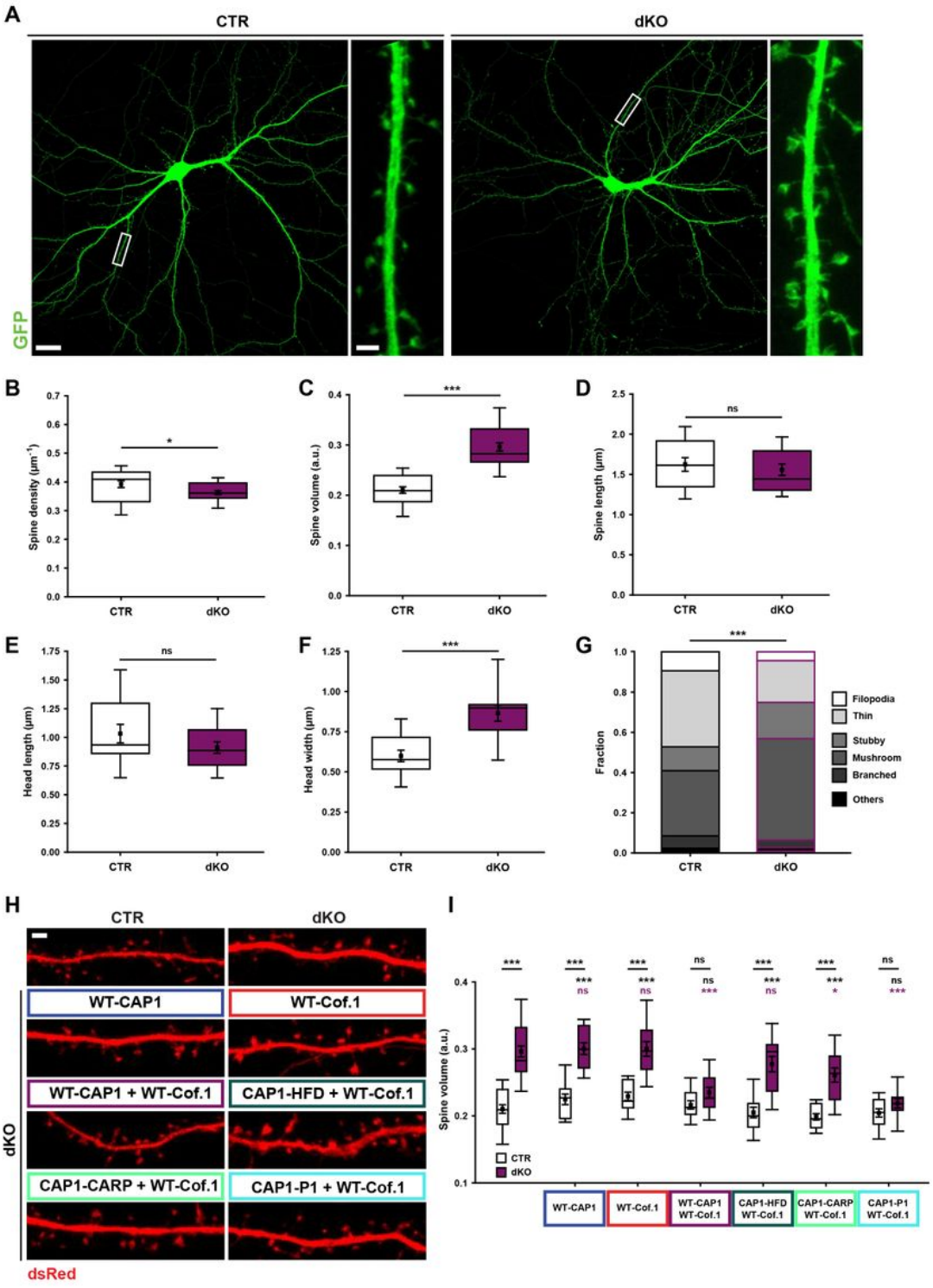

Figure 8

Figure 8

Functional interdependence of CAP1 and cofilin1 in spines. (A) 10 Micrographs of GFP-expressing CTR and double-KO (dKO) neurons. Boxes indicate areas shown with higher magnification. Graphs showing (B) spine density, (C) spine volume, (D) total spine length, (E) spine head length and (F) spine head width in CTR and dKO neurons. (G) Graph showing relative fraction of spine types in CTR and dKO neurons. (H) Micrographs showing dsRed in CTR neurons as well as in dKO neurons upon transfection of CAP1 and/or cofilin1 constructs as indicated. (I) Graph showing spine volume in CTR and dKO neurons upon expression of WT-cofilin1 and/or CAP1 constructs as indicated. Black asterisks and ns above dKO values indicate significance of changes when compared to CTR (furthest left values), purple asterisks and ns above dKO values indicate significance of changes when compared to double mutant neurons (second values from left). Scale bars (μm): 2 (A, high magnification, H), 20 (A, overview). ns: $P \geq 0.05$, *: $P < 0.05$, ***: $P < 0.001$.

Supplementary Files

This is a list of supplementary files associated with this preprint. Click to download.

- FigureS1.jpg
- FigureS2.jpg
- FigureS3.jpg
- FigureS4.jpg
- FigureS5.jpg
- MovieS1.avi
- MovieS2.avi
- TableS1.pdf
- TableS2.pdf
- TableS3.pdf